



Sensitivity of aerosol retrieval to geometrical configuration of ground-based sun/sky radiometer observations

B. Torres^{1,2}, O. Dubovik², C. Toledano¹, A. Berjon³, V. E. Cachorro¹, T. Lapyonok², P. Litvinov², and P. Goloub²

¹Group of Atmospheric Optics, Valladolid University, Valladolid, Spain

²Laboratoire d'Optique Atmosphérique, Université des Sciences et Technologies de Lille, Villeneuve d'Ascq, France

³Izana Atmospheric Research Center, Spanish Meteorological Agency, Tenerife, Spain

Correspondence to: B. Torres (benjamin@goa.uva.es)

Received: 13 February 2013 – Published in Atmos. Chem. Phys. Discuss.: 14 March 2013

Revised: 25 November 2013 – Accepted: 6 December 2013 – Published: 24 January 2014

Abstract. A sensitivity study of aerosol retrievals to the geometrical configuration of the ground-based sky radiometer observations is carried out through inversion tests. Specifically, this study is focused on principal plane and almucantar observations, since these geometries are employed in AERONET (AErosol RObotic NETwork). The following effects have been analyzed with simulated data for both geometries: sensitivity of the retrieval to variability of the observed scattering angle range, uncertainties in the assumptions of the aerosol vertical distribution, surface reflectance, possible instrument pointing errors, and the effects of the finite field of view. The synthetic observations of radiometer in the tests were calculated using a previous climatology data set of retrieved aerosol properties over three AERONET sites: Mongu (Zambia) for biomass burning aerosol, Goddard Space Flight Center (GSFC; Maryland, USA) for urban aerosol and Solar Village (Saudi Arabia) for desert dust aerosol. The results show that almucantar retrievals, in general, are more reliable than principal plane retrievals in presence of the analyzed error sources. This fact partially can be explained by practical advantages of the almucantar geometry: the symmetry between its left and right branches that helps to eliminate some observational uncertainties and the constant value of optical mass during the measurements, that make almucantar observations nearly independent of the vertical variability of aerosol. Nevertheless, almucantar retrievals present instabilities at high sun elevations due to the reduction of the scattering angle range coverage, resulting in decrease of information content. It is in such conditions that principal plane retrievals show a better stability, as shown by the simulation analysis of the three different aerosol models.

The last part of the study is devoted to the identification of possible differences between the aerosol retrieval results obtained from real AERONET data using both geometries. In particular, we have compared AERONET retrievals at the same sites used in the simulation analysis: Mongu (biomass burning), GSFC (urban) and Solar Village (desert dust). Overall, this analysis shows robust consistency between the retrievals from simultaneous observations in principle plane and almucantar. All identified differences are within the uncertainties estimated for the AERONET operational aerosol retrieval. The differences in the size distribution are generally under 10 % for radii between 0.1 μm and 5 μm , and outside this size range, the differences can be as large as 50 %. For the absorption parameters, i.e., single scattering albedo and the imaginary part of the refractive index, the differences are typically under 0.01 and 0.003, respectively. The real part of the refractive index showed a difference of 0.01 for biomass burning and urban aerosol, and a difference of around 0.03 for desert dust. Finally, it should be noted that the whole data set includes only 200 pairs, which have been taken under very stable atmospheric conditions; therefore, in a general case, differences between principal plane (PPL) and almucantar (ALM) are expected to be higher. Though the observed differences between ALM and PPL are rather small, it should be noted that this analysis has been conducted using a limited set of 200 observation pairs selected under stable atmospheric conditions.

1 Introduction

In the past decades, atmospheric aerosol has been widely recognized as an atmospheric constituent important not only for the understanding of atmospheric processes, but also as one of the factors impacting many different aspects of the life on Earth (Solomon et al., 2007; IPCC, 2007). Indeed, the aerosol directly impacts ecosystems and human health as a pollutant (generated by industrialization and fossil fuel combustion). It has also been recognized for its influence on the global climate system. This effect is known as “aerosol radiative forcing”, and includes the so-called direct effects (basically scattering and absorption of solar radiation), as well as indirect effects, created by the modification of cloud properties (cloud lifetime, cloud albedo, precipitation, chemistry, etc.).

The aerosol particles can be natural (sea salt, desert dust, volcanic ash) or anthropogenic (nitrates, sulfates, organics, carbonaceous, etc.), or a mixture of both, with particle sizes ranging from a few nanometers to hundreds of micrometers; this leads to a complex and heterogeneous system with different physical, chemical and optical properties (Willeke and Baron, 1993; D’Almeida et al., 1991). This complexity makes it necessary to take a multidisciplinary approach to studying aerosol, one which implies the integrated use of very different methods and techniques.

In this context, this paper is focused on the analysis of the important features of aerosol columnar properties retrieval from radiometric observations. This approach is based on the analysis of the light resulting from the interaction of solar radiation with the aerosol particles suspended in the atmosphere. The high spatial and temporal variability of the aerosol properties has led to the development and establishment of measurement networks covering extensive areas. Among all the monitoring systems, ground-based observations have been revealed as the most accurate and simplest. The most important ground-based global remote sensing networks are AERONET (AErosol RObotic NETwork) (Holben et al., 1998), SKYNET (Takamura and Nakajima, 2004) and PFR-GAW (Precision Filter Radiometer-Global Atmosphere Watch) (Wehrli, 2005).

AERONET and SKYNET networks provide aerosol information from two kinds of spectral measurements: spectral data of direct Sun radiation attenuation by the atmosphere and angular distribution of diffuse sky radiation, while PFR-GAW only provides data of direct Sun radiation. The direct measurements provide information about total aerosol loading, i.e. AOD (aerosol optical depth). The observations of diffuse radiation contain essential information for retrieving the aerosol phase function and optical aerosol properties. Using this information, important aerosol optical and microphysical parameters, such as the particle size distribution (Nakajima et al., 1983, 1996) and complex refractive index or single scattering albedo (Dubovik and King, 2000; Dubovik et al., 2006), are derived.

The present work aims at identifying whether the retrieval results depend on the geometry used in the sky radiance measurements. In particular, this work has been carried out with the inversion algorithm described in Dubovik and King (2000) (also Dubovik et al., 2000, 2002, 2006), and using data provided by AERONET. That is why the study will be focused on the almucantar and principal plane geometries (hereafter, ALM and PPL respectively), that are adapted (Holben et al., 1998; Kaufman et al., 2002; Olmo et al., 2008) as the standard observational scenarios in operational data acquisition of the AERONET network (Holben et al., 1998). Also, the same observational scenarios are used by SKYNET (Nakajima et al., 1996).

In the almucantar configuration, Fig. 1 on the left, the sun photometers (e.g., Cimel Electronique 318, standard in AERONET) keep the zenith angle constant (equal to the solar zenith angle θ_s). The azimuth movement is done first towards the right (taking the Sun as reference and up to $\varphi_a = 180^\circ$) and then is repeated towards the left. Assuming a homogeneous atmosphere, the measurements taken in both right and left branches are expected to be symmetrical and the final radiance values used in the inversion algorithm for the almucantar are obtained by averaging the observations in the right and left branches. This process allows elimination of the data contaminated by sky inhomogeneities. In AERONET network processing, the symmetry property in almucantar has been used for over a decade, and those measurements exhibiting radiance differences higher than 20 % between right and left branches are eliminated (this and other quality control criteria are described in http://aeronet.gsfc.nasa.gov/new_web/Documents/AERONETcriteria_final1_excerpt.pdf and Holben et al., 2006).

In the principal plane geometry (Fig. 1 on the right), the azimuth angle is the one that remains constant while the zenith angle varies. Note that this geometry does not present any evident symmetry and, therefore, identifying and screening sky inhomogeneities in principal plane observations is not straightforward.

Another important aspect that distinguishes ALM and PPL geometries is the relation between the scattering angle Θ , the solar zenith angle θ_s and the observation angles θ_a and φ_p for almucantar and principal plane, respectively. For any measurement, the scattering angle can be expressed as $\cos(\Theta) = \cos^2(\theta_s) + \sin^2(\theta_s) \cos(\varphi_a - \varphi_s)$ for the almucantar¹, and $\cos(\Theta) = \cos(\theta_p \mp \theta_s)$ for the principal plane² (Nakajima et al., 1996). As a consequence, the maximum scattering angle that can be reached in both geometries is

¹Normally, the azimuth origin is taken in the Sun position and therefore $\varphi_s = 0$. Note that this assumption was made in Fig. 1.

²The signs (–) in the case of ($\varphi_p - \varphi_s = 0^\circ$) and (+) for the case of ($\varphi_p - \varphi_s = 180^\circ$).

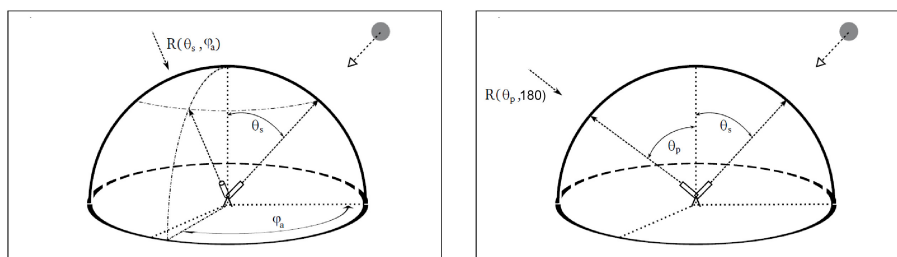


Fig. 1. Figures describing the two geometries used within AERONET network for the measurements of the sky radiances; the almucantar is shown on the left, the principal plane is shown on the right.

$\Theta_M = 2\theta_s$ in the almucantar and $\Theta_M = \theta_s + 90^\circ$ in the principal plane³.

This fact plays an important role in the present study, as the information contained in the radiance measurement critically depends on the geometry selected, especially for small values of the solar zenith angle. Specifically, the first part of this work contains an analysis of the consequences of having different ranges of scattering angle coverage in ALM and PPL measurements. For that purpose, in Sect. 2 we use simulated sky radiances for different θ_s and aerosol types which will be inverted afterwards to observe the differences in the retrievals. In the same section, we include an analysis of the effect of neglecting the vertical variability of aerosol and its effects in both geometries. Additionally, we study the influence of some other aspects that could affect ALM and PPL in a different way, such as an uncertainties in the surface reflectance assumption, the effect of an incorrect pointing in both geometries and the effect of considering a finite field of view. Finally, we examine whether or not the results obtained in the simulation are supported by real observations. For this purpose, we analyze the differences in the retrievals obtained from nearly simultaneous principal plane and almucantar measurements, selected under stable atmospheric conditions, at the same key sites.

2 Analysis of simulated data

2.1 Methodology and data

In the first section, we study the variability of the retrievals for different solar zenith angles corresponding to different

ranges of scattering angle coverage in ALM and PPL measurements. Also, in order to assure the reliability of our studies, we have conducted self-consistency tests of the inversion code. First, we simulate radiance measurements with the forward module using the pertinent size distribution (columnar volume size distribution $dV/d\ln(R)$ for radii between 0.05–15 μm) and the refractive index of the different aerosol examples. Then these synthetic observations are inverted using the retrieval algorithm and the resulting values are compared with the assumed aerosol properties. The tests are conducted for both PPL and ALM geometries. A scheme of this procedure is drawn in Fig. 2. The test conditions, which are the solar zenith angles (five cases: $\theta_s=15^\circ, 30^\circ, 45^\circ, 60^\circ$ and 75°) and the measurement geometry (almucantar or principal plane), are also included in the diagram.

This strategy for conducting the sensitivity studies has been adapted from a previous work by Dubovik et al. (2000). The principal novelty here is the testing of the reliability of principal plane retrievals and the comparison of those retrievals with retrievals from almucantar observations. In addition, for modeling the aerosol properties, we used climatology of real aerosol retrievals from AERONET observations (described in Dubovik and King, 2000; Dubovik et al., 2006), and Dubovik et al., 2002) instead of using aerosol models found in sparse literature. In that climatology analysis, characteristics of different aerosol types observed at several AERONET key sites are derived as a function of the aerosol optical depth. Specifically, we have taken the information from three sites: Mongu (Zambia) for biomass burning aerosol, Goddard Space Flight Center (GSFC; Maryland, USA) for urban aerosol and Solar Village (Saudi Arabia) for desert dust aerosol. For these three examples, two possibilities for the aerosol load have been considered: the first one around the averaged value of the aerosol optical depth (registered in the study Dubovik et al., 2002), and the second one with more aerosol load so as to see if certain conditions affect differently as the aerosol load increases.

Table 1 summarizes the aerosol properties of the all the examples considered. We provide the full set of parameters needed to run the forward module. The first parameter is the reference value of the aerosol optical depth from which the rest of the input parameters are derived (using the

³It should be noted that operationally observations cannot be made all the way to the horizon due to horizon obstructions and also due to inexact optical air mass computations (refraction effects, etc.). Therefore, the maximum scattering angle in the principal plane scan is typically smaller than stated theoretically (e.g., in AERONET, the Level 2 AOD product is limited to a maximum air mass of 5 as the effect of atmosphere sphericity is not negligible for larger air masses and this is not accounted in the plane-parallel radiative transfer model used for aerosol retrieval (Dubovik and King, 2000). Therefore, $\Theta_M \simeq \theta_s + 80^\circ$).

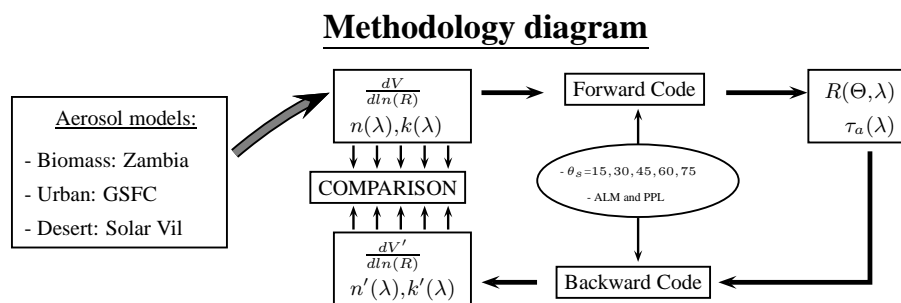


Fig. 2. Methodology diagram followed to carry out the self-consistency test of the code used for different aerosol types, solar zenith angles and geometries for measuring the sky radiance.

expressions in Dubovik et al., 2002). The next parameters in Table 1 are used to describe the size distribution (modeled as a bimodal lognormal function): particle volume concentration (C_{Vi} [$\mu\text{m}^3/\mu\text{m}^2$]), volume median radius (r_{Vi} [μm]) and mode width (σ_{Vi}) for fine and coarse mode. The remaining inputs are the refractive index and the sphericity parameter, which is taken as 0 for desert dust (all the particles are considered to be non-spherical) and in the rest of the cases as 100 (considering all the particles as spheres).

The simulated aerosol optical depth and the single scattering albedo are shown in the output part of Table 1. It should be noted that the obtained spectral aerosol optical depth obtained using Dubovik et al. (2002) dynamic models is slightly different from the entry values used for generating full optical properties. This can be explained by the fact that aerosol models from Dubovik et al. (2002) are based on the linear regression analysis, and, therefore, an exact match between the entry optical thickness ($\tau_{a_{\text{ref}}}$ in Table 1) and simulated optical thickness τ_a is not expected. Indeed, the aerosol optical depth depends nonlinearly on such aerosol parameters as real and imaginary parts of the refractive index, and therefore, the regression analysis is just an approximation. In addition, here the calculation for the desert dust has been made using the spheroid package developed by Dubovik et al. (2006) while retrieval obtained by Dubovik et al. (2002) was based on the retrieval that used only spherical assumption. As a result, we see a slightly higher discrepancy between entry and output values of optical thickness, even though, generally, simulations of extinction do not almost depend on shape of large particles. For example, if we considered the spherical model for the desert dust type in the forward simulations, the values for the aerosol optical depth at 1020 nm for SolV1 and SolV2 would be $\tau_a(1020) = 0.294$ and $\tau_a(1020) = 0.493$. These values are in better agreement with the reference values and the differences could then be related to the mentioned non-linear dependencies. Also note that these simulated values do not depend on the “conditions” such as the measurement geometry or the solar zenith angle. Finally, we should remark here that larger AOD implies better retrieval accuracy; however, we have decided to maintain the typical aver-

age values for each site (even though they are quite different) so that our study is related to the average conditions.

In addition to the consistency check and analysis of dependence on the solar zenith angle, the same methodology is also used to analyze the sensitivity to different error sources (see the flowchart in Fig. 2). For example, in order to study the influence of the pointing error, we simulate the radiances by introducing an incorrect pointing. Subsequently, these synthetic data are inverted and, the obtained results compared with the ones assumed to be “true”.

2.2 Dependence on the solar zenith angle

The results of the consistency tests are shown in Fig. 3 for the three aerosol types considered: biomass burning aerosol (Fig. 3a), urban aerosol (Fig. 3b) and desert dust aerosol (Fig. 3c). The study is made following the scheme presented in Fig. 2. In addition to the size distribution and the refractive index (the parameters that drive the forward simulations), the single scattering albedo is also illustrated, due to its great significance. The results retrieved with the almucantar geometry are shown in the upper part, while results from simulations with the principal plane are placed at the bottom of every subfigure. In all the representations, the results obtained for the case with smallest aerosol load (e.g., desert dust: $\tau_{a_{\text{ref}}}(1020) = 0.3$) are plotted with a solid line while dashed line is used for the case with the largest aerosol load (e.g., desert dust $\tau_{a_{\text{ref}}}(1020) = 0.5$).

Size distributions are represented in the subfigures on the left. The “true” size distribution used for producing the synthetic observations is plotted in black. The size distributions produced from inversion of synthetic data are plotted in different colors, depending on the solar zenith angle used for the simulations: dark blue for 15° , light blue for 30° , green for 45° , orange for 60° , and brown for 75° .

The optical parameters, single scattering albedo, and the refractive index are plotted as a function of the solar zenith angle. Different colors have been chosen, in this case, for different wavelengths – blue for 440 nm, green for 670 nm, yellow for 870 nm, and red for 1020 nm. The input values

Table 1. Description of aerosol properties used for simulating the radiance measurements. The first row specifies the parameters describing the size distribution which is modeled as a bimodal lognormal function: C_{V_i} [$\mu\text{m}^3/\mu\text{m}^2$], r_{V_i} [μm] and σ_{V_i} . Refractive index and the sphericity parameter are also parts of the input. Single-scattering albedo and aerosol optical depth, for each wavelength, are shown as the output after applying the forward model.

Biomass burning (Zambia)								
INPUT	$\tau_{a_{\text{ref}}}(440)$	r_{V_f}	σ_{V_f}	C_{V_f}	r_{V_c}	σ_{V_c}	C_{V_c}	$Sph.$
– Zamb1 –	0.400	0.130	0.400	0.048	3.504	0.730	0.004	100
– Zamb2 –	0.800	0.140	0.400	0.096	3.788	0.730	0.007	100
	$n(440)$	$n(670)$	$n(870)$	$n(1020)$	$k(440)$	$k(670)$	$k(870)$	$k(1020)$
– Zamb1 –	1.5100	1.5100	1.5100	1.5100	0.0210	0.0210	0.0210	0.0210
– Zamb2 –	1.5100	1.5100	1.5100	1.5100	0.0210	0.0210	0.0210	0.0210
OUTPUT	$\tau_a(440)$	$\tau_a(670)$	$\tau_a(870)$	$\tau_a(1020)$	$\omega_o(440)$	$\omega_o(670)$	$\omega_o(870)$	$\omega_o(1020)$
– Zamb1 –	0.416	0.184	0.107	0.078	0.8778	0.8290	0.7811	0.7467
– Zamb2 –	0.872	0.397	0.232	0.167	0.8827	0.8402	0.7958	0.7620
Urban (GSFC)								
INPUT	$\tau_{a_{\text{ref}}}(440)$	r_{V_f}	σ_{V_f}	C_{V_f}	r_{V_c}	σ_{V_c}	C_{V_c}	$Sph.$
– GSFC1 –	0.200	0.142	0.380	0.030	3.128	0.790	0.018	100
– GSFC2 –	0.500	0.175	0.380	0.075	3.275	0.790	0.030	100
	$n(440)$	$n(670)$	$n(870)$	$n(1020)$	$k(440)$	$k(670)$	$k(870)$	$k(1020)$
– GSFC1 –	1.4100	1.4100	1.4100	1.4100	0.0030	0.0030	0.0030	0.0030
– GSFC2 –	1.4100	1.4100	1.4100	1.4100	0.0030	0.0030	0.0030	0.0030
OUTPUT	$\tau_a(440)$	$\tau_a(670)$	$\tau_a(870)$	$\tau_a(1020)$	$\omega_o(440)$	$\omega_o(670)$	$\omega_o(870)$	$\omega_o(1020)$
– GSFC1 –	0.195	0.083	0.048	0.036	0.9718	0.9588	0.9476	0.9404
– GSFC2 –	0.559	0.254	0.145	0.102	0.9771	0.9691	0.9604	0.9535
Desert dust (Solar Village)								
INPUT	$\tau_{a_{\text{ref}}}(1020)$	r_{V_f}	σ_{V_f}	C_{V_f}	r_{V_c}	σ_{V_c}	C_{V_c}	$Sph.$
– SolV1 –	0.300	0.120	0.400	0.026	2.320	0.600	0.274	0
– SolV2 –	0.500	0.120	0.400	0.030	2.320	0.600	0.470	0
	$n(440)$	$n(670)$	$n(870)$	$n(1020)$	$k(440)$	$k(670)$	$k(870)$	$k(1020)$
– SolV1 –	1.5600	1.5600	1.5600	1.5600	0.0029	0.0013	0.0010	0.0010
– SolV2 –	1.5600	1.5600	1.5600	1.5600	0.0029	0.0013	0.0010	0.0010
OUTPUT	$\tau_a(440)$	$\tau_a(670)$	$\tau_a(870)$	$\tau_a(1020)$	$\omega_o(440)$	$\omega_o(670)$	$\omega_o(870)$	$\omega_o(1020)$
– SolV1 –	0.483	0.371	0.344	0.332	0.9300	0.9664	0.9772	0.9794
– SolV2 –	0.707	0.591	0.568	0.557	0.9209	0.9647	0.9768	0.9793

are not shown in order to make the interpretation of the figure easier; they can be seen in Table 1.

The most evident tendency observed in the tests is the instability of the optical parameters for small solar zenith angles in the almucantar. This tendency is present in the tests for all aerosol types. For instance, the single scattering albedo differs on average around 0.02 at $\theta_s = 15^\circ$ from those obtained at larger solar zenith angle. This latter agrees with the values given in Table 1. On the other hand, the results obtained with the principal plane geometry do not have such

strong dependence on the solar zenith angle. The values are shown in Table 1.

The instability in the retrievals obtained from almucantar data can be explained by the fact that only aerosol scattering in middle and large scattering angles depends on a complex index of refraction and the forward peak of aerosol phase function is dominated by light diffraction (Bohren and Huffman, 1983). In this regard, the maximum scattering angle for almucantar observational geometry is $2\theta_s$, i.e., the measurements corresponding to small solar zenith angles do not

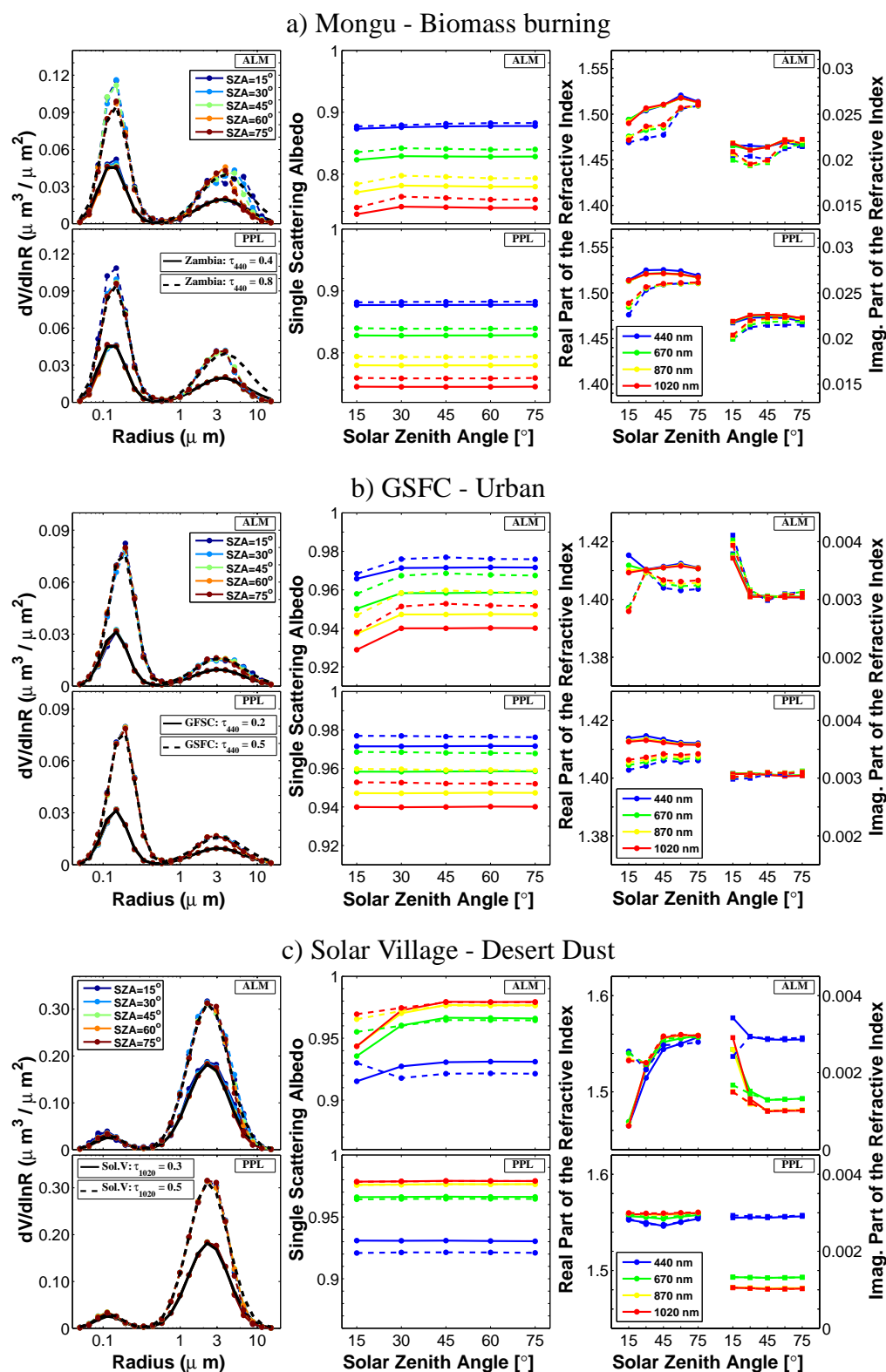


Fig. 3. Summary of the aerosol retrievals obtained in the self-consistency test using three aerosol types: biomass burning aerosol (a), urban aerosol (b) and desert dust aerosol (c) with two different AOD utilized as references in each case (solid line used for the case with smallest aerosol load and dashed line for the largest). For every subfigure, almucantar results are shown in the upper part whereas principal plane results are presented in the bottom part. Figures on the left correspond to size distribution results. Figures in the center illustrate the results for the single scattering albedo, and figures on the right describe the results for the complex refractive index.

contain enough information to adequately retrieve the index of refraction or, consequently, the single scattering albedo. The same result was described for simulations in Dubovik et al. (2000).

In the refractive index analysis, we observe the same result; for the principal plane, the retrievals are stable and the values correspond to those given in Table 1 (the only exception is found for the case of the biomass burning at $\theta_s = 15^\circ$). On the other hand, the retrievals obtained for the almucantar drift further apart from their input values as the solar zenith angle becomes smaller. The worst-case behavior can be found with desert dust with low aerosol load, where the real part of refractive index is 0.1 smaller than the assumed value at $\theta_s = 15^\circ$ (1.46 when it should be 1.56), and the imaginary part is much higher than the inputs, especially for long wavelengths where values are three times larger.

From the analysis of the differences in the size distribution, a dependency on the radius can be seen: the differences observed between the retrievals and the input values do not exceed 10 % for intermediate radii (in both retrievals ALM and PPL) while they strongly increase in the extremes. In the cases of urban and desert dust, these intermediate radii range only between 0.1 μm and 5 μm , while for biomass burning the range is smaller: between 0.3 μm and 3 μm . Moreover, the differences between the input values and the retrievals (and between the retrievals themselves, i.e. PPL vs. ALM) are much higher for the case of biomass burning (which are over 100 %) than for urban and desert dust (which are only up to 40 %).

The analysis of the differences for the biomass burning, illustrated in Fig. 3, shows noticeable differences in the fine mode only when the maximum scattering angle is smaller than 120° ($\theta_s = 15^\circ, 30^\circ, 45^\circ$ for almucantar and $\theta_s = 15^\circ$ for the principal plane simulations), and especially for the case with larger aerosol load (named Zamb2) where the values of the size distribution become unexpectedly higher than the original size distribution (up to 20 %). This effect is accompanied by a sharp decline in the real refractive index (from 1.51 to 1.47–1.48). Both effects compensate each other for the calculation of optical thickness; there are more particles but they scatter less light. There is a strong connection between the retrieved fine mode and the real part of the refractive index, as they are both more sensitive to the large angles of the phase function. This effect has been already seen in previous works (Dubovik et al., 2002; Sinyuk et al., 2007; Li et al., 2009) and will be recurrent in the next sections. Nevertheless, the discrepancies are more striking in the coarse mode. For principal plane, all the size distributions are separated from the original one when the radius is higher than 3 μm . They all have the same values and decrease faster than the input for radii above 3 μm . For the almucantar, nonetheless, the size distributions also diverge from the original but they do not have a defined direction.

The larger discrepancies in the extremes can be explained by the very low sensitivity of radiometer observations to the

size distribution variation for the radius smaller than 0.1 μm or larger than 3 μm for the wavelengths used in AERONET (Dubovik et al., 2000). Particularly for the case of biomass burning, this effect gets more important, since its coarse mode is displaced towards larger radii (r_{vc} for Mongu site is the largest among the selected examples) while for the other examples the volume concentration in this size region is quite lower. Finally, we conclude that the tests did not reveal any systematic pattern of differences between the retrievals obtained through PPL and ALM. The larger noise in the extremes compare to that for the central radii is the only effect observed.

2.3 Dependence on the aerosol vertical distribution

Once the discrepancies obtained due to the different scattering angle coverage of both geometries are analyzed, the next step is the study of the influence of some other aspects that could affect ALM and PPL differently. First we analyze the effect of the aerosol vertical distribution variability in the atmosphere. As mentioned in the introduction and illustrated in Fig. 1, the zenith angle is kept constant during measurement in the almucantar, and the observation in the almucantar has a symmetry whereas principal plane does not.

The second, and less obvious, characteristic of observations in the almucantar is their low dependence on the aerosol vertical variability, which is generally weaker than that for observations in principle plane. This can be illustrated with the following brief analysis of solution of radiative transfer equation in single-scattering approximations for almucantar and principle plane geometries.

Let us consider the solution of the radiance R for the first-order scattering and for any observation angle θ_v given by

$$R = \frac{F_0}{|\mu_v|} e^{-\tau/|\mu_v|} \times \int_0^{z_t} \left(\sum_k M_k \right) e^{-m' t(z)} dz, \quad (1)$$

where F_0 is the extraterrestrial irradiance and

$$\tau = \int_0^{z_t} \sum_k \sigma_{\text{ext}_k}(z) dz$$

$$t(z) = \int_0^z \sum_k \sigma_{\text{ext}_k}(z') dz'$$

$$M_k = \frac{\omega_{ok} P_k \sigma_{\text{ext}_k}(z)}{4\pi}$$

$$m' = \frac{1}{\mu_s} - \frac{1}{|\mu_v|}; \text{ with } \mu_s = 1/\cos\theta_s \text{ and } \mu_v = 1/\cos\theta_v$$

Observe that we have included k components at any height, z , of the atmosphere. The parameters P_k (redefined as $P_k = P_k/4\pi$) and σ_{ext_k} are, respectively, the phase function and the extinction coefficient for every single component. However, in the almucantar, observations $\mu_s = \mu_v$ and

Eq. (1) should be rewritten as

$$R_a = \frac{F_0}{\mu_s} e^{-\tau/\mu_s} \times \int_0^{z_t} \left(\sum_k M_k \right) dz. \quad (2)$$

The phase function, P_k , and the single scattering albedo, $\omega_{ok}(z)$, for every single component do not depend on the height and can be taken out of the integral.

$$R_a = \frac{F_0}{\mu_s} e^{-\tau/\mu_s} \times \left(\sum_k \omega_{ok} \tau_k P_k \right), \quad (3)$$

where

$$\tau_k = \int_0^{z_t} \sigma_{extk}(z) dz. \quad (4)$$

Equation (3) is already independent from the height. Therefore, for the single-scattering approximation in the almucantar geometry, the radiance measurements do not depend on the vertical distribution of the components in the atmosphere, particularly not on the aerosol vertical distribution.

Note that, as is typical, we consider three main components: gaseous absorption, molecular scattering (Rayleigh), and aerosol scattering and absorption, and Eq. (3) is rewritten as

$$R_a = \frac{F_0}{\mu_s} e^{-\tau/\mu_s} [\omega_o \tau_a P_a + \tau_R P_R], \quad (5)$$

with

$$\tau = \tau_{abs}^{gas} + \tau_{scat}^a + \tau_{abs}^a + \tau_R. \quad (6)$$

The exponential term within the integral in the general equation, Eq. (1), links the principal plane measurement to the aerosol and gas vertical distribution. Only in the case that we consider just one main layer in the atmosphere (without any changes in the vertical distribution) could we deduce a similar expression for the principal plane as in Eq. (5),

$$R_p = \frac{F_0 \mu_s}{\mu_v - \mu_s} \left[\frac{\omega_o \tau_a P_a + \tau_R P_R}{\tau_a + \tau_R} \right] \left[e^{-\frac{\tau}{\mu_v}} - e^{-\frac{\tau}{\mu_s}} \right]. \quad (7)$$

Consequently, in the single-scattering approximation, a heterogeneous aerosol vertical distribution would only affect the principal plane. Multiple scattering effects of the light in the atmosphere add some sensitivity to vertical variability of atmosphere for both observations in the almucantar and in the principal plane. Nonetheless, since the transmitted radiation of aerosol is dominated by the effects of the first order of scattering, the dependence of radiances in the almucantar on the vertical variability of the atmosphere is generally weaker than that for radiances measured in principal plane.

The above conclusion suggests that some differences between aerosol retrievals from simultaneous measurements in principle plane and almucantar can appear due to their different sensitivities to the assumptions regarding aerosol vertical distribution. This aspect is of particular interest for the

present study because generally there is no reliable information for making accurate assumptions about aerosol vertical distribution. Only in situations when co-located data from the lidar are available is accounting for detailed aerosol vertical distribution possible (e.g., Lopatin et al., 2013).

To analyze the effects of the vertical distribution, we produced synthetic observations using the aerosol properties of urban (GSFC2) and desert dust (SolV2). The forward calculations were conducted using the assumption of a multilayered plane parallel atmosphere: 30 layers, equidistant in pressure, were used. Utilizing the same idea as in Sinyuk et al. (2007), we used two different aerosol vertical distributions: two Gaussian profiles with 1 km width, one with at ground level and the other with an aerosol concentration profile median height at 3 km (Sinyuk et al., 2007, Fig. 1). To check the possible dependency of the results on θ_s , we have done the tests for $\theta_s = 45^\circ$ and $\theta_s = 75^\circ$. First, the simulated radiances for both geometries were inverted under the assumption of a monolayered atmosphere. This assumption is used in operational AERONET (Dubovik and King, 2000) and SKYNET processing (Nakajima et al., 1996).

Figure 4 represents the size distributions retrieved under the previously mentioned conditions for urban (left) and desert dust (right) aerosol types. Note that in total, there are eight size distributions for each aerosol case, corresponding to every possible combination between the two geometries, the two vertical aerosol profiles, and the two solar zenith angles.

The results obtained are quite similar for both aerosol types. For almucantar geometry, the size distributions retrieved do not display any significant differences compared to the assumed “true” values. Only small differences can be observed in the coarse mode for desert dust at $\theta_s = 75^\circ$, where the effect of multiple scattering is more important. The maximum of these differences is observed for $r = 3 \mu\text{m}$ with a value around 10 %. By contrast, principal plane results show two interesting tendencies: on the one hand, the results for $\theta_s = 45^\circ$ do not significantly differ from the input size distributions for both aerosol types; on the other hand, they present important differences in the case of $\theta_s = 75^\circ$, especially for the fine mode, where they reach values over 50 %.

This interesting result confirms the theoretical expectations foreseen above: the principal plane retrievals are more likely affected by aerosol vertical distribution than almucantar inversions. The simulations reveal the larger differences with the assumed values for the geometries with large solar zenith angles, especially for the size distribution in the fine mode. The retrieval errors appear to be larger when the aerosol concentration profile median height is assumed to be at ground level than when it is at 3 km.

If the vertical structure of the aerosol is known, the accurate aerosol profile can be used in the retrieval. In such conditions, all retrieved properties can adequately be retrieved from both geometries. Figure 5 shows the results for the retrieval using accurate vertical profile for the case of urban

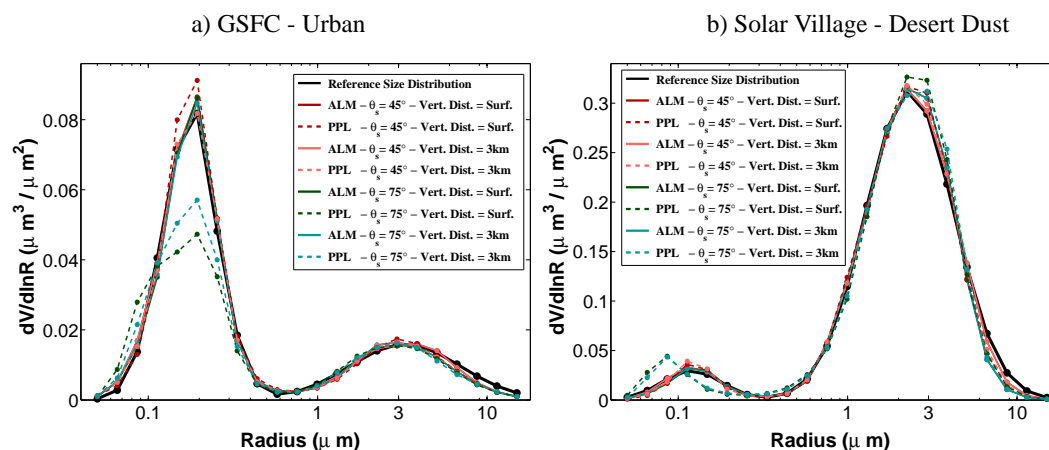


Fig. 4. Aerosol size distributions retrieved in the study of the influence on the aerosol vertical profiles. Using the aerosol properties of urban (a) and desert dust (b), radiance measurements have been previously simulated for the two geometries, almucantar (solid line) and principal plane (dashed line), considering 30 layers in the atmosphere. During the retrieving process, only one layer has been used in the four analyzed cases: $\theta_s = 45^\circ$ and vertical profile centered in the Earth surface (red lines), $\theta_s = 45^\circ$ and vertical profile centered at $h = 3$ km (pink lines), $\theta_s = 75^\circ$ and vertical profile centered in the Earth surface (green lines), $\theta_s = 75^\circ$ and vertical profile centered at $h = 3$ km (blue lines).

aerosol at $\theta_s = 75^\circ$ measured in principal plane. The subfigure on the left represents the case with aerosol concentration profile median height at ground level, and the subfigure on the right represents the case with the maximum at 3 km. Red and blue lines denote the retrievals for the case in which the atmosphere is assumed to have two layers and five layers, respectively, defining the border between layers as equidistant in pressure.

In practice, however, accurate information about vertical distribution of the aerosol is rarely available, whereas the vertical profile may change quite dramatically. Therefore, in this study we are interested in finding out whether taking into account at least some general features characteristics for the vertical distribution of the atmosphere may reveal any advantages in comparison to using the base assumption of monolayered atmosphere. With that purpose, we first investigated the effect of straightforward reduction of vertical resolution of multilayered atmosphere (assuming correct aerosol profile in the inversion). The assumption of bilayered atmosphere substantially improves the results compared to monolayered atmosphere retrievals (shown in Fig. 4), especially for the case in which the aerosol concentration profile median height is at 3 km (where the errors are practically negligible). In the case when the aerosol median height is at the ground level, the errors are around 20 %, but they diminish as the number of assumed layers is increased. For instance, if the retrieval is provided with five layers, the errors are under 5 % for both cases.

Nevertheless, the above tests were done using the known vertical profile of aerosol, which generally is not known. Therefore, in the second series of tests, we have focused on the evaluation of the possibility to use generic assumption of bilayered atmosphere where the lower layer contains

aerosol mixed with Rayleigh scattering while the upper layer contains only Rayleigh scattering. Indeed, in the real atmosphere, molecular scattering generally dominates at altitudes above ~ 5 km (Fig. 6 in Elterman, 1966 and Table 4.10 in D’Almeida et al., 1991, and references therein). In Fig. 5, gray lines represent these alternative solutions: solid line when the border between the layers is fixed at 2 km, dashed line when the border is at 4 km, and dash-dotted when it is at 6 km.

Using the second assumption leads to generally worse results compared to retrievals obtained using accurate aerosol vertical distribution. Furthermore, there is no an optimum choice of the altitude at which to put the border between the two layers. Thus, in the first representation, i.e., the case with the maximum aerosol concentrations at ground level, the border assumption providing the best results was the one located at 2 km, and the size distributions retrieved deteriorated with the increase of the border altitude. On the other hand, the case with the maximum aerosol concentrations at 3 km showed the opposite tendency, and the results improved with increase of the border of layer altitude.

Previously, we have only shown the results for the case $\theta_s = 75^\circ$, but the addition of a second layer improves the results of $\theta_s = 45^\circ$ as well. Thus, the maximum errors found in central radii diminish from 10 % to 5 % when the border is situated at 4 km. Note that the selection of the border altitude between the layers is not an easy task. Apparently, the placement of border layer at around 4 km is an excellent compromise for the two examples presented here. Nevertheless, this height could be particularly chosen for each specific site, taking into the account several factors, for instance, the altitude of site, or whether or not the surrounding area is a source of aerosol, etc.

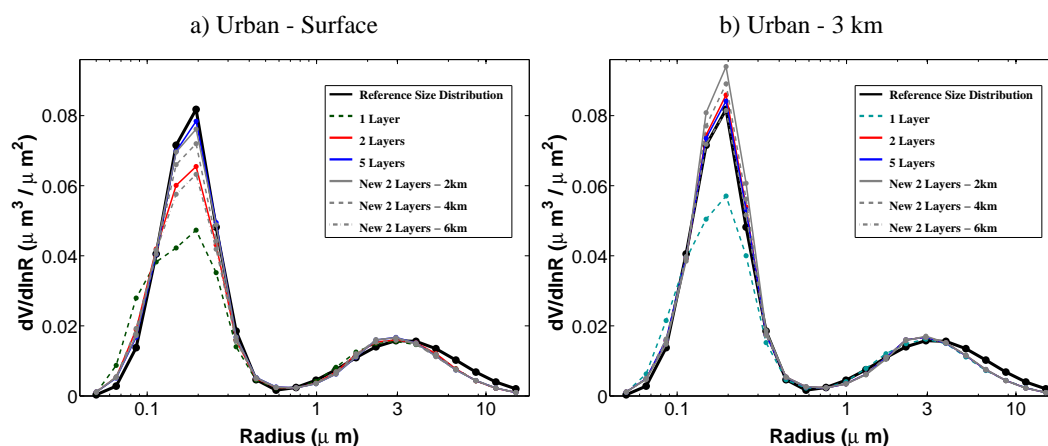


Fig. 5. Aerosol size distributions retrieved considering more than one layer for principal plane geometry in the case of urban aerosol at $\theta_s = 75^\circ$. **(a)** Contains the results for the case with aerosol concentration profile median height at ground level, and **(b)** for the case with the maximum at 3 km. Red and blue lines represent the cases for two layers and five layers, respectively (the layers being equidistant in pressure), with the description of the aerosol vertical profile known during the retrieval process. Gray lines represent the alternative solutions when the vertical profile is unknown: solid line when the border between the layers aerosol–non aerosol is fixed at 2 km, dashed line when the border is at 4 km and dash-dotted when is at 6 km.

Finally, we should mention the discussion of this section was focused on the retrieval of aerosol size distribution, because the retrieval of this property showed that it was the most sensitive to the assumption regarding the vertical structure of the atmosphere. For the other optical parameters, the results can be summarized by two basic observations. First, neither the retrieval of single scattering albedo nor of the imaginary part of the refractive index showed any sensitivity to the vertical variability of aerosol. Second, the retrieval of the real part of the refractive index for fine mode does show some sensitivity to the vertical variability of aerosol. However, these deviations in real part of the refractive index strongly anti-correlate with the fine mode aerosol concentration (the smaller refractive index, the larger the concentration) and this effect disappears under the same conditions when the retrieval errors are diminished for the size distribution retrieval.

To illustrate both tendencies, we have represented, in Table 2 the optical parameters retrieved for the case that has shown the greatest errors in the present study: urban aerosol at $\theta_s = 75^\circ$ with the aerosol vertical distribution with maximum at the surface. As noted previously, there are no differences for single scattering albedo and the imaginary part of the refractive index, while differences up to 0.12 are observed for the real part. The maximum differences are observed when monolayered atmosphere model is employed in the retrieval. When the aerosol vertical distribution is known, the addition of layers reduces the error. Note that for five layers the differences are already in the third decimal.

For the cases without extra information about the aerosol vertical profile, the strategy of the two layers described here provides the same results as for the size distribution. In this

particular case, when the border is situated at 2 km there are almost no differences, and as the border becomes higher the differences appear. Nevertheless, the proposed intermediate solution of settling the border at 4 km still presents acceptable differences around 0.01 in the real part of the refractive index.

Thus, overall the tests showed that for inversions of the radiances measured in almucantar the vertical variability of aerosol is not an issue, and assumption of monolayered atmosphere does not result in any notable retrieval errors. This conclusion can also be extended to the aerosol retrieval from principle plane with a unique exception of the observations at the large solar zenith angles. At the same time, for the last scenario, the retrieval errors can be practically eliminated by assuming generic bilayered aerosol + Rayleigh/Rayleigh atmosphere. These conclusions support the retrieval settings adapted for operational retrieval in the AERONET network: the aerosol vertical distribution is assumed homogeneous in the almucantar inversion and bilayered for the principal plane inversion. (http://aeronet.gsfc.nasa.gov/new_web/Documents/Inversion_products_V2.pdf).

2.4 Dependence on the surface reflectance

The second aspect under discussion will be dependence on the surface reflectance for both geometries. With this purpose, we will introduce a random error in the surface reflectance during the inversion procedure in order to study the effects on the retrievals. In its current version, AERONET Version 2, the inversion algorithm (described in Dubovik and King, 2000, and Dubovik et al., 2006) approximates the surface reflectance by a bidirectional reflectance function (BRDF). The Cox–Munk model

Table 2. Retrieved aerosol optical parameters considering different numbers of atmosphere layers. The aerosol type considered is the urban aerosol at $\theta_s = 75^\circ$ with the aerosol vertical distribution with maximum at the surface.

	440 nm			670 nm			870 nm			1020 nm		
	n	k	ω_o	n	k	ω_o	n	k	ω_o	n	k	ω_o
Reference	1.410	0.003	0.977	1.410	0.003	0.969	1.410	0.003	0.960	1.410	0.003	0.954
1 layer	1.519	0.003	0.977	1.494	0.003	0.970	1.487	0.003	0.961	1.484	0.003	0.955
2 layers	1.439	0.003	0.977	1.431	0.003	0.969	1.428	0.003	0.960	1.427	0.003	0.953
5 layers	1.411	0.003	0.976	1.411	0.003	0.968	1.411	0.003	0.959	1.412	0.003	0.952
2 layers, 2 km	1.410	0.003	0.976	1.410	0.003	0.968	1.411	0.003	0.959	1.411	0.003	0.952
2 layers, 4 km	1.422	0.003	0.977	1.419	0.003	0.969	1.418	0.003	0.960	1.418	0.003	0.953
2 layers, 6 km	1.440	0.003	0.978	1.433	0.003	0.970	1.431	0.003	0.961	1.431	0.003	0.954

is used for retrievals over water (Cox and Munk, 1954) and the Lie–Ross model over land (Lucht and Roujean, 2000). This surface description is also currently used in AERONET retrievals (http://aeronet.gsfc.nasa.gov/new_web/Documents/Inversion_products_V2.pdf).

The BDRF parameters are basically three – $f_{\text{iso}}(\lambda)$, $f_{\text{vol}}(\lambda)$ and $f_{\text{geom}}(\lambda)$; they characterize the isotropic, volumetric, and geometric optics surface scattering, respectively (Roujean et al., 1992; Wanner et al., 1995 and Litvinov et al., 2011). In AERONET version 2 retrievals (Holben et al., 2006; Eck et al., 2008), the land BDRF parameters are adopted from MODIS Ecotype generic BDRF models and mixed with the ecosystem map of Moody et al. (2005): geographically and temporally varying (16 day averages throughout the annual cycle) surface albedos are utilized. These spectral surface albedos are midday black sky albedos from Moody et al. (2005), and are based on atmospherically corrected MODIS data averaged over a 5 km radius of each AERONET site (see Eck et al., 2008; Sect. 2.3). The BDRF model and parameters (for each ecosystem type) are used to compute the spectral reflectances at solar zenith angles throughout the day over a 5 km radius of each AERONET site (see Eck et al., 2008; Sect. 2.3). The BDRF model and parameters (for each ecosystem type) are used to compute the spectral reflectances at solar zenith angles throughout the day.

The following scheme is used for the tests: first radiances are simulated (as in Fig. 2) with the typical BDRF parameters observed in the three sites (see Table 3). Subsequently, the data are inverted for 200 different scenarios using BDRF parameters perturbed by Gaussian noise. Specifically, the errors in f_{iso} will be relative errors generated randomly from a normal distribution with mean 0 and standard deviation of 15 %, with a limit of ± 30 %. The errors in f_{vol} and f_{geom} will be absolute errors generated randomly, and with values of the standard deviations of 0.05 and 0.025 respectively; the error limits will be established as ± 0.1 for f_{vol} (with $f_{\text{vol}} > 0$) and 0.05 for f_{geom} (with $f_{\text{vol}}, f_{\text{geom}} > 0$). Note that we have considered a general case with random error even though the BDRF model based on several ecosystem types could have

biases for different geographical locations and therefore bias errors are likely to be significant in some conditions.

In the illustrations of the results, we focus on the analysis of the cases (from Table 1) with the largest aerosol load for the three aerosol types; as in the previous section, we will only evaluate the cases at $\theta_s = 45^\circ$ and $\theta_s = 75^\circ$.

Figures 6 and 7 depict the means and the standard deviations of the differences between the 200 retrievals and the non-error case. The results are shown for principal plane and almucantar geometry and for each aerosol type: biomass burning (Zamb2, at the top), urban (GSFC2, in the middle) and desert dust (SolV2, at the bottom). Relative differences have been used for the analyses of the size distribution (figures in the left), while the differences in the optical parameters are provided in absolute terms.

Analyzing the outcomes, there are two results that stand out from the rest. First, there is not a clearly defined tendency in the mean of the differences, as could be expected, because in our analysis only random errors were considered. In the size distribution, for instance, the means rarely exceed 10 % and their signs do not follow a clear pattern. In the optical parameters the means are also very small; in this way, the maximum mean of the absolute difference for the single scattering albedo is 0.003. Therefore, the analysis needs to be carried out in terms of the standard deviation, which contains, in this case, the information about the dependency of the retrieved products on a random error in the surface reflectance. Secondly, and from this new approach, it can be seen that the error in the surface reflectance affects more at $\theta_s = 45^\circ$ than at $\theta_s = 75^\circ$. The last result is even more evident for the principal plane geometry, as will be further discussed. For instance, if we start the study with the size distribution, while in the almucantar we observe a small improvement of the results from $\theta_s = 45^\circ$ to $\theta_s = 75^\circ$, the improvement in the principal plane is considerably more obvious.

The highest values of the means and the standard deviations are observed for the fine mode for desert dust and urban aerosols at $\theta_s = 45^\circ$, as commented. For both cases, all the standard deviations for radii smaller than $0.3 \mu\text{m}$ are over 10 %, reaching the maximum of 22 % at $0.07 \mu\text{m}$ in the desert

Table 3. Values of $f_{\text{iso}}(\lambda)$, $f_{\text{vol}}(\lambda)$ and $f_{\text{geom}}(\lambda)$ used to approximate the surface reflectance by a bidirectional reflectance function (BDRF) in the sites used in the simulations Mongu, Goddard and Solar Village.

	440 nm			670 nm			870 nm			1020 nm		
	f_{iso}	f_{vol}	f_{geom}	f_{iso}	f_{vol}	f_{geom}	f_{iso}	f_{vol}	f_{geom}	f_{iso}	f_{vol}	f_{geom}
Mongu (dry season)	0.064	0.026	0.010	0.147	0.076	0.024	0.274	0.173	0.029	0.311	0.196	0.033
Goddard (winter)	0.032	0.008	0.003	0.092	0.035	0.011	0.209	0.234	0.033	0.232	0.227	0.032
Solar Village	0.161	0.074	0.024	0.405	0.217	0.057	0.445	0.272	0.037	0.479	0.293	0.040

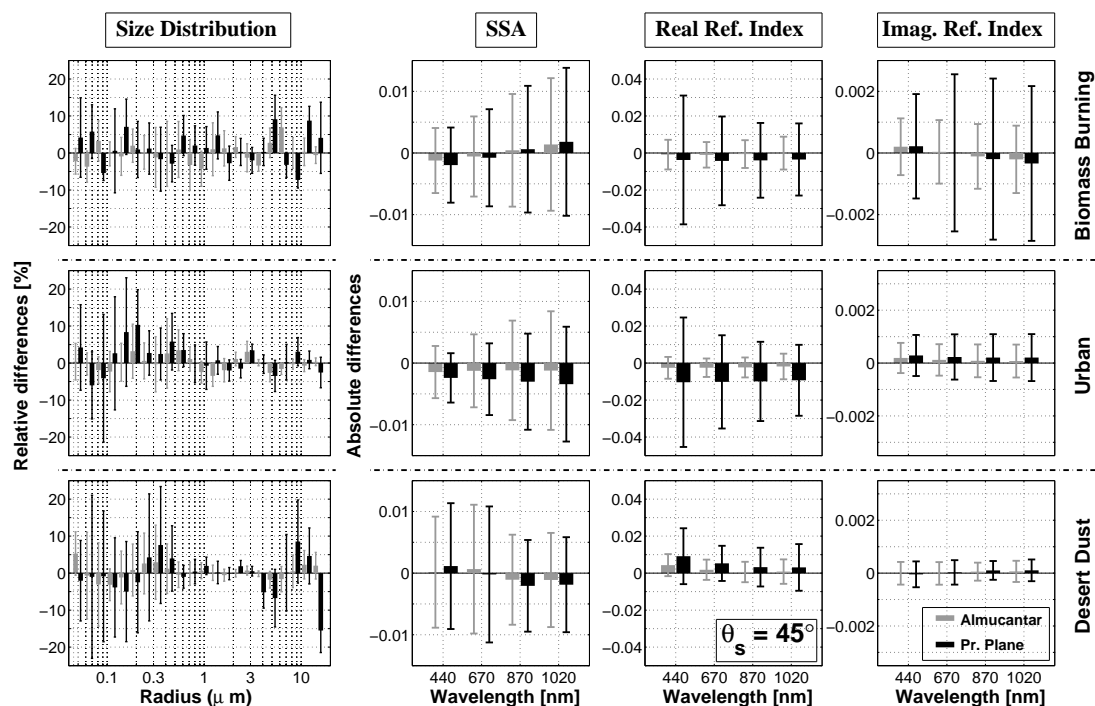


Fig. 6. Means and the standard deviations of the differences between the 200 retrievals, where Gaussian errors are introduced in the BDRF parameters, and the non-error case at $\theta_s = 45^\circ$. Figures at the top correspond to biomass burning aerosol, in the middle to urban aerosol, and at the bottom to desert dust aerosol. Relative differences are used for the analyses of the size distribution (figures in the left), while the differences in the optical parameters are provided in absolute terms. Results are shown for almucantar (gray) and for principal plane (black) geometry.

dust. For larger radii, both the means and the standard deviations of the differences are reduced (the latter rarely exceeds 5 % when the radii are larger than $0.3 \mu\text{m}$); the only exception is the relative large values observed for the principal plane when radii are larger than $5 \mu\text{m}$. On the other hand, the results for biomass burning do not depend on the radii. In this case, the maximum values of the means are around 8 % and the standard deviation is about 12 %.

As mentioned above, the retrieval results are more accurate at $\theta_s = 75^\circ$. The means of the differences are smaller than 5 % in the urban and in the biomass burning. For the desert dust, there are some values of the principal plane retrievals in the fine mode and some values of the almucantar retrievals in the coarse mode which are larger than the 5 %. In fact, the

results for the almucantar retrieval of the coarse mode are worse than they are at $\theta_s = 45^\circ$.

In the single scattering albedo the means of the differences are smaller than 0.003 for all the simulations. The standard deviations are similar for the three aerosol cases, being the maximum values around 0.013, reached at $\theta_s = 45^\circ$. It can be also observed that the principal plane values are slightly higher than the almucantar ones. Following the general outcome, the results are better at $\theta_s = 75^\circ$, with the maximum of the standard deviations being 0.008. The improvement is more notorious in the principal plane resulting in lower values of the standard deviations than almucantar at this solar zenith angle.

A similar result is found for the refractive index; at $\theta_s = 45^\circ$, the results for almucantar retrieval are better, while at

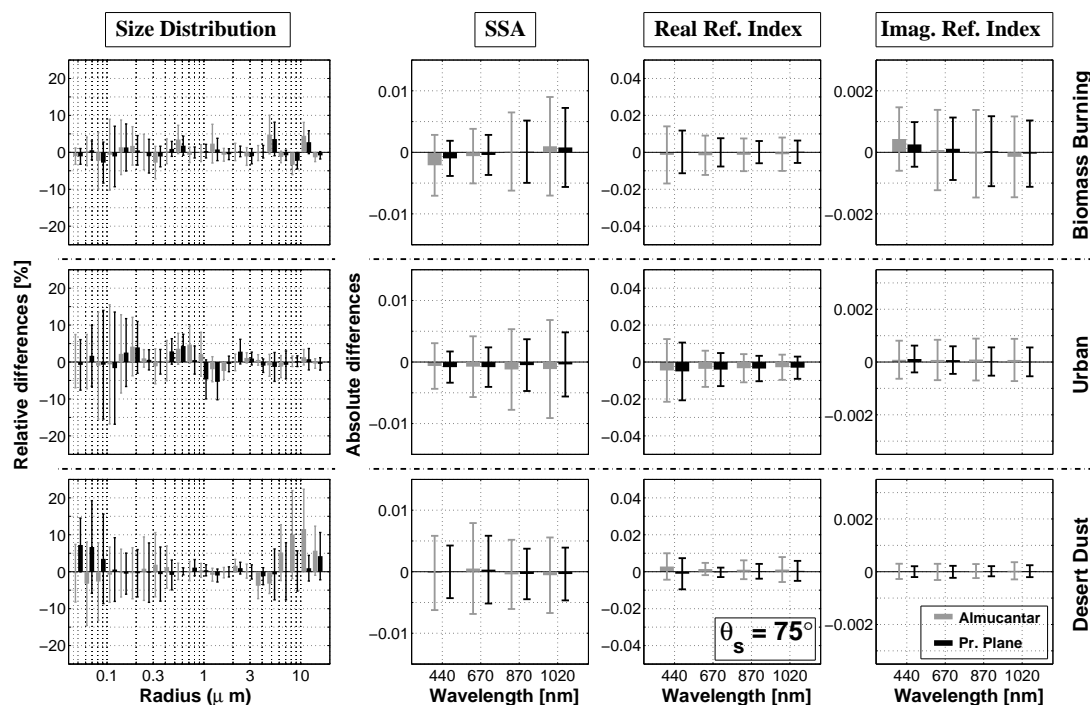


Fig. 7. Means and standard deviations of the differences between the 200 retrievals, where Gaussian errors are introduced in the BDRF parameters, and the non-error case at $\theta_s = 75^\circ$. Figures at the top correspond to biomass burning aerosol, those in the middle to urban aerosol, and those at the bottom to desert dust aerosol. Relative differences are used for the analyses of the size distribution (figures in the left), while the differences in the optical parameters are provided in absolute terms. Results are shown for almucantar (gray) and for principal plane (black) geometry.

$\theta_s = 75^\circ$ they are not as good as the principal plane ones. For the real part, the maximum of the standard deviation is around 0.03 at $\theta_s = 45^\circ$ (reached in principal plane geometry) and around 0.02 (reached in almucantar geometry).

For the imaginary part, the biomass burning case shows larger standard deviations than the other two cases, due to its larger absorption. The maxima at $\theta_s = 45^\circ$ and at $\theta_s = 75^\circ$ are reached for this aerosol type, with values 0.0028 and 0.0015, respectively. For urban and desert dust, the standard deviations are smaller than 0.001 for both solar zenith angles.

In summary, the introduction of a random noise in the BDRF parameters affects all the analyzed aerosol properties more at $\theta_s = 45^\circ$ than at $\theta_s = 75^\circ$. This is more evident in the case of the principal plane geometry, which presents higher differences at $\theta_s = 45^\circ$ than the almucantar geometry, while at $\theta_s = 75^\circ$ the differences are similar for both geometries (even slightly smaller for the principal plane geometry).

2.5 Dependence on the pointing error

The pointing error is defined as the angle between the Sun position (correct pointing) and the erroneous pointing direction. As sun photometers are moved by two motors, azimuth and zenith axes, the value of the pointing error, Θ_ξ , is nor-

mally given in spherical coordinates:

$$\Theta_\xi = \Theta_\xi(\xi_\varphi, \xi_\theta), \quad (8)$$

where ξ_φ and ξ_θ are the error components in azimuth and zenith angles, respectively. Assuming that the pointing error is sufficiently small, it can be expressed as an infinitesimal displacement in spherical coordinates (with $dr = 0$) and therefore the relation in Eq. (8) takes the following form:

$$\Theta_\xi = \xi_\theta \hat{\theta} + \sin \theta_s \xi_\varphi \hat{\varphi} = \sqrt{\xi_\theta^2 + \sin^2 \theta_s \xi_\varphi^2}. \quad (9)$$

The work by Torres et al. (2013) (also in Torres, 2012) describes a methodology used for the characterization of these magnitudes and a first evaluation of the results for several individual instruments (all of them Cimel 318 sun photometers). One of the main outcomes of this evaluation is that the magnitudes ξ_θ and $\sin \theta_s \xi_\varphi$ are constant for each photometer, regardless of θ_s . This result indicates that the pointing error, Θ_ξ , can be understood as the scattering angle between the Sun beam and the direction in which the detector (in charge of the Sun pointing-process in the instrument) is pointing, which is constant through the day. In the present work, the characteristic magnitudes $\Theta_{\xi\theta} = \xi_\theta$ and $\Theta_{\xi\varphi} = \sin \theta_s \xi_\varphi$, will be called the total vertical and horizontal error, respectively, keeping the names zenith and azimuth error for ξ_θ and ξ_φ .

respectively. The first tests on this topic, done with seven photometers in the work by Torres et al. (2013), showed that for most of the instruments the magnitudes of ξ_θ and $\sin\theta_s\xi_\varphi$ were smaller than 0.1° . The maximum values obtained for vertical and horizontal error were 0.25° , while the maximum of the total error, Θ_ξ , was 0.3° .

The scheme for this study is similar to the one presented in Fig. 2, but introduces the pointing errors in the forward code. The value of the simulated pointing error will be 0.4° (horizontal and vertical) as it is the maximum realistic error that can be committed without affecting the aerosol optical depth and therefore not noticeable in the data obtained from AERONET network (the value of the field of view is around 1.2° in the standard sun photometers of the network). Note that in the work by Torres (2012), the retrieval errors for 0.2° and 1° are also analyzed; one of the most important results obtained in that study is that differences in the retrievals can be neglected in the case of 0.2° , which means that the typical pointing errors (under 0.1°) do not have any significant influence in AERONET retrievals. The results obtained for the case of 1° are also depicted in Torres (2012), and they were not included in the present study as they do not represent a realistic error. Here, the value of 0.4° will be considered for positive or negative errors in the vertical component and only positive errors in the horizontal component.

The vertical error can be committed from the Sun towards the zenith or towards the Earth surface; these two possibilities result in different consequences in almucantar and principal plane measurements, and therefore both of them should be considered. In this study, the sign of the error is established as positive in the case of variation towards the zenith, and negative in the case of variation towards the Earth surface. The horizontal error can be committed either to the left or to the right of the Sun. In the principal plane, regardless of the error direction, the consequences are symmetric. In the almucantar, the errors are initially not symmetric, but due to the possibility of averaging the left and right branches (as it is done operationally in AERONET), they become symmetric. As a consequence, for both geometries, there is no need to consider the sign of the horizontal error and only the absolute value is relevant. Note also that the averaging process produces that in the almucantar the horizontal error effect is much weaker than in the principal plane.

The results of the simulations of the pointing error test are presented in Fig. 8 for the size distribution, in Fig. 9 for the single scattering albedo, and in Fig. 10 for the refractive index. In each figure, the results are depicted for the three aerosol types considered: biomass burning aerosol (subfigure a), urban aerosol (subfigure b) and desert dust aerosol (subfigure c). For each aerosol type, results retrieved with the almucantar geometry are shown in the upper part, while results from simulations with the principal plane are placed at the bottom. The subfigures on the left correspond to retrievals with vertical errors (positive and negative), and the ones on the right to horizontal errors (only positive). Note

that the x axis is the radius for the size distribution and different colors represent different solar zenith angle; for the optical parameters the x axis is precisely the solar zenith angle and the colors distinguish between the wavelengths.

Analyzing Fig. 8, the first thing we observe is that there are only remarkable differences with respect to the results obtained in Fig. 3 for the cases involving principal plane and vertical errors; i.e., there are no differences in the almucantar regardless of the error pointing type, nor are there differences in the principal plane with horizontal error.

Centering the study on the case with vertical errors in PPL, the aerosol type showing the largest differences is desert dust, where for the case with a positive vertical error there is a 10 % decrease in the size distributions between $1\mu\text{m}$ and $3\mu\text{m}$ and a little increment around 4–5 % for larger radii. With negative vertical error, the situation is the opposite; there is a big increase (up to 15–20 %) for radii between $1\mu\text{m}$ and $3\mu\text{m}$, accompanied by a significant reduction for larger radii.

In the other two aerosol cases, and especially for urban aerosol, we can see the behavior of the fine mode, which is opposite to that of the coarse mode: it grows for positive errors and decreases for negative errors. To be more precise, the perturbations are only observed for radii smaller than $0.3\mu\text{m}$, and in general, they are smaller than the ones found in the coarse mode. Moreover, the differences between the results found here and the ones obtained in Sect. 2.2 depend on θ_s and on the aerosol load being larger as both parameters are smaller. The values of these differences are normally under 20 %. However, the maximum values are around 50 %, and they are found for the urban case at $\theta_s = 15^\circ$ with the lowest aerosol load and at radii between 0.05 and $0.2\mu\text{m}$.

To explain these results, we need to check the differences in the radiance measurements that the pointing errors generate. For this purpose, radiance relative differences are represented in Fig. 11 – for vertical errors in almucantar and principal plane in the upper part, and for horizontal errors in the subfigures at the bottom. We have only taken the differences for GSFC aerosol not to be repetitive, as there are no relevant differences respect to the other aerosol types. Note also that the differences are plotted against the scattering angle and at different θ_s (from left to the right at 15° , 45° and 75°).

The relative differences generated by vertical errors in the principal plane (see Fig. 11) are five times larger than the ones originated in the almucantar and a magnitude order larger than the differences generated by horizontal errors in both geometries. This fact explains why the largest differences found in Fig. 8 are for vertical errors in principal plane geometry. We also observe that the results for positive and negative vertical errors are symmetric in the principal plane (not in the almucantar). These differences are positive for small scattering angles when the errors are negative, and they are negative for positive errors. At large scattering angles the relation is the opposite: positive for positive errors and negative for negative errors.

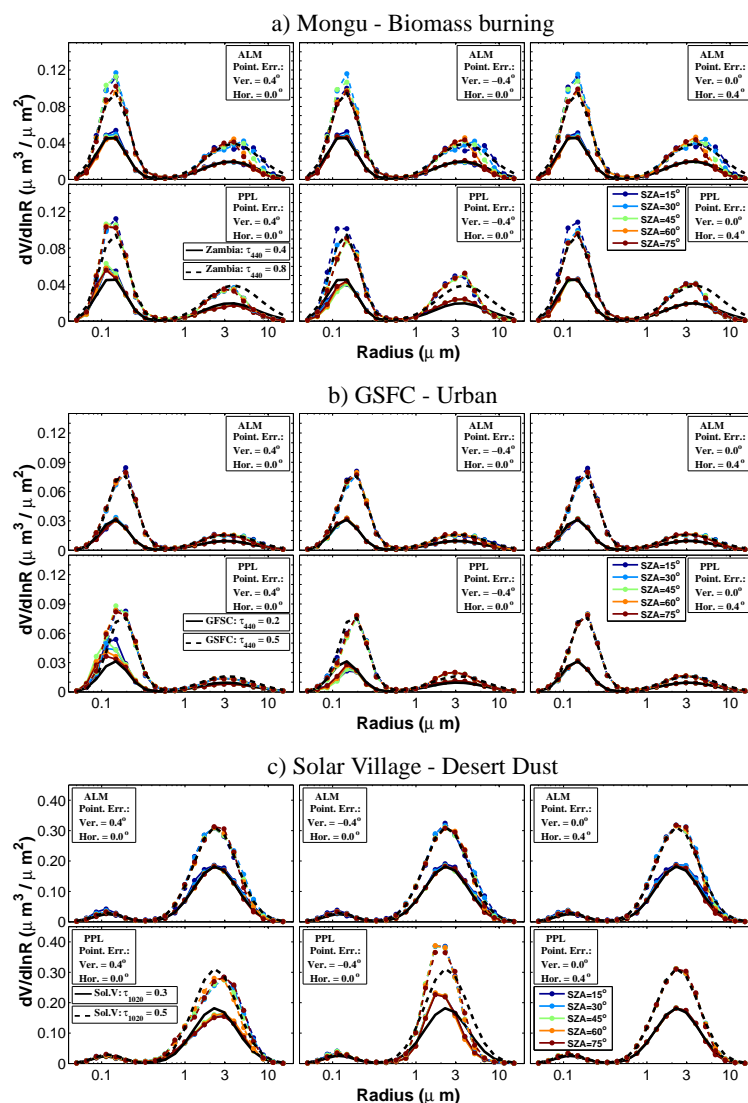


Fig. 8. Retrieved size distributions after simulating a pointing error of 0.4° in three different aerosol types: biomass burning aerosol (a), urban aerosol (b) and desert dust aerosol (c) with two different AODs as references in each case (solid line used for the case with smallest aerosol load and dashed line for the largest). In each of the figures, the subfigures at the top show results from almucantars and those at the bottom from principal planes. Subfigures on the left correspond to retrievals with vertical errors, and those on the right correspond to horizontal errors. Colors indicate the solar zenith angle: dark blue for $\theta_s = 15^\circ$, light blue for $\theta_s = 30^\circ$, green for $\theta_s = 45^\circ$, orange for $\theta_s = 60^\circ$ and brown for $\theta_s = 75^\circ$, while black is used for the original size distributions.

The coarse mode of the size distribution is more connected to small scattering angles, while the information about fine particles is more equally distributed. An increase of radiation for small scattering angle is interpreted by the inversion code as an increase of the coarse mode, while an increase in the backscattered radiation is interpreted as an enlargement of the fine mode. Therefore, when the vertical errors in principal plane geometry are positive, there is decrease in the radiance at small scattering angles and an increase at large scattering angles which is the cause of the observed decrease in the coarse mode and increase in the fine mode. The negative errors generate opposite effects in the radiance, which

creates the contrary effect in the size distribution to the one we observed in Fig. 8.

The next step in the study is the analysis of the differences in the ω_0 and in the refractive index. As we commented in the Sect. 2.2, the optical properties are connected to all the scattering angles. Single scattering albedo and imaginary refractive index are closely related. Moreover, since our simulations keep the aerosol optical depth constant, an increase of radiance will mean more scattering compared to the absorption and therefore, ω_0 will rise while the imaginary part of refractive index will fall. The opposite situation will occur for less radiance: ω_0 will decrease due to the reduction of

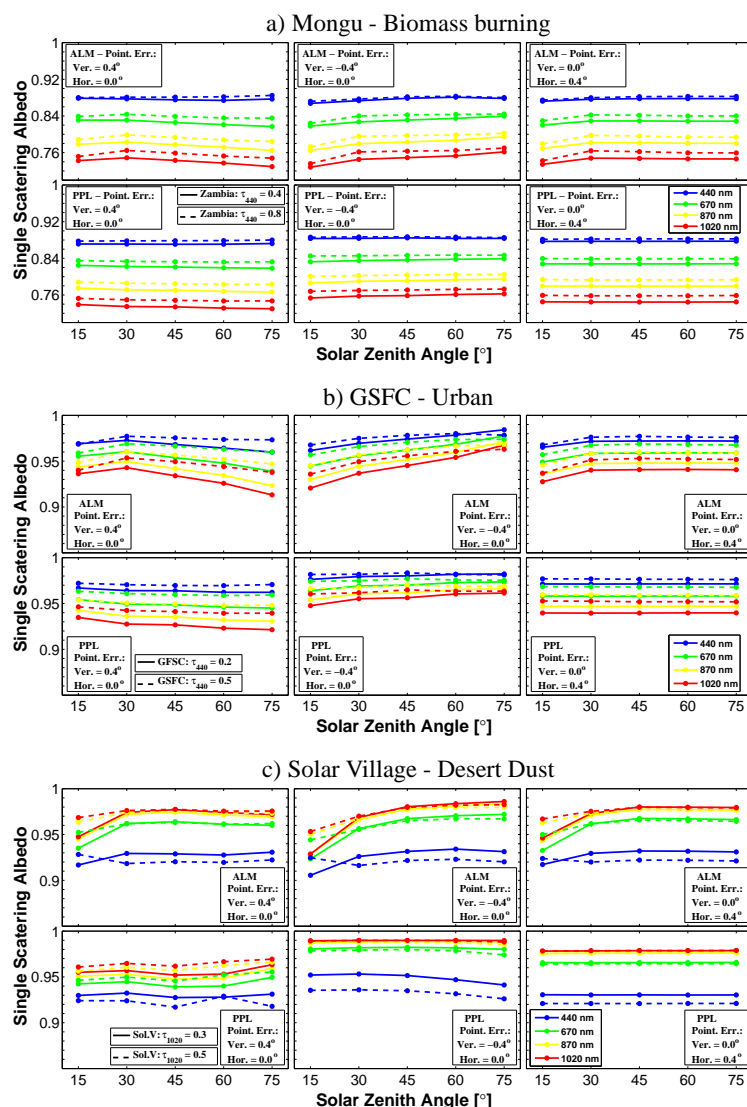


Fig. 9. Retrieved single scattering albedo after simulating a pointing error of 0.4° in three different aerosol types: biomass burning aerosol (a), urban aerosol (b) and desert dust aerosol (c) with two different AOD as reference in each case (solid line used for the case with smallest aerosol load and dashed line for the largest). In each of the figures, subfigures on top show results from almucantars and at the bottom from principal planes. Subfigures on the left correspond to retrievals with vertical errors, and on the right, to horizontal errors. Colors indicate the wavelength: blue for 440 nm, green for 670 nm, yellow for 870 nm and red for 1020 nm.

the scattered light and the imaginary refractive index will rise because of a larger absorption. The real part of the refractive index is more connected with the shape of the radiance. High values of radiance for small scattering angles and low values for large angles are related to low values of the real refractive index. The opposite situation will mean high values in the real refractive index.

Referring back to Fig. 11, the radiance differences in the principal plane produced by positive vertical pointing errors are mostly negative, especially for small scattering angles. Based on this, we can expect the single scattering albedo to decrease and the imaginary part of refractive index to in-

crease. Expectancies for the consequences of negative errors are just the opposite. Taking a quick look at Figs. 9 and 10 we see that our expectations were correct: Fig. 9 shows that ω_0 drops for positive errors and grows for negative errors. Here, it is interesting to note that these variations are greater for the case with less aerosol load in the three examples; in the same manner, the differences are smaller as the aerosol is more absorptive. Maximum differences of 0.02 are found for desert dust while the minimum differences, which are smaller than 0.01, are reached in the biomass burning.

The presence of positive vertical error in the principal plane geometry diminishes the radiance at small scattering

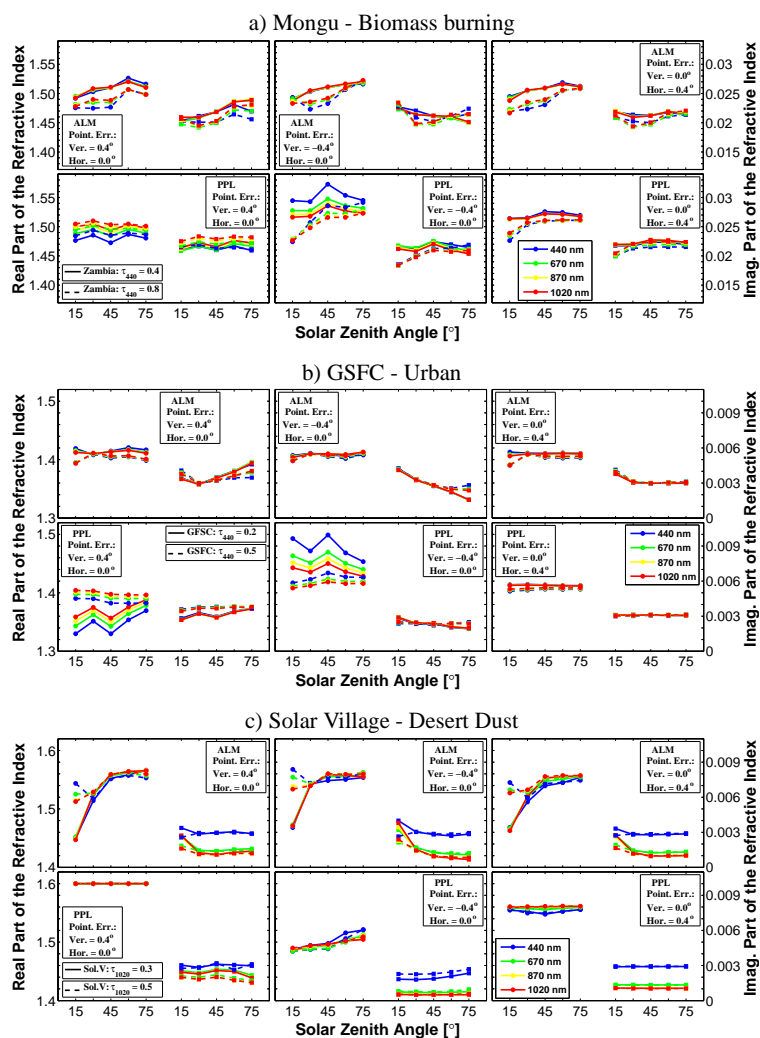


Fig. 10. Retrieved refractive index after simulating a pointing error of 0.4° in three different aerosol types: biomass burning aerosol (a), urban aerosol (b) and desert dust aerosol (c) with two different AOD as reference in each case (solid line used for the case with smallest aerosol load and dashed line for the largest). In each of the figures, subfigures on top show results from almucantars and at the bottom from principal planes. Subfigures on the left correspond to retrievals with vertical errors, and on the right, to horizontal errors. Colors indicate the wavelength: blue for 440 nm, green for 670 nm, yellow for 870 nm and red for 1020 nm. The y axes express the real refractive index (on the left) and the imaginary refractive index (on the right).

angles, while at the other angles, there is no variation. For negative errors we observe the opposite result. Due to this fact, the real part of refractive index is expected to enlarge (or to shrink for negative) to a great extent. And this is exactly what it is found to do in the desert dust example where the real part rises from 1.56 to the highest value (1.6) allowed by the inversion process in all the channels. For the negative error, it falls to values between 1.49 and 1.52, varying with the channel and the θ_s .

However, for the other two aerosol types, the real part of the refractive index decreases for a positive error, which is contrary the previous argument. It should be remembered that this idea was used successfully in the desert dust case and, as the radiance differences in all the cases present the

same behavior, apparently there is no immediate explanation for the different behavior. A possible explanation could be obtained by analyzing the size distributions; in the desert dust case for positive vertical errors, the retrievals from principal planes gave a decrease of the coarse mode and no variations in the fine mode. More light for longer scattering angle with less particles could be only explained with a strong increase in the real refractive index. But for urban and biomass burning examples, the fine mode increases for vertical pointing errors. In this second scenario, if the increment of the particles is very strong, even in the case of more light, the real refractive index can drop even more if we consider the strong connection between real part of refractive index and the fine

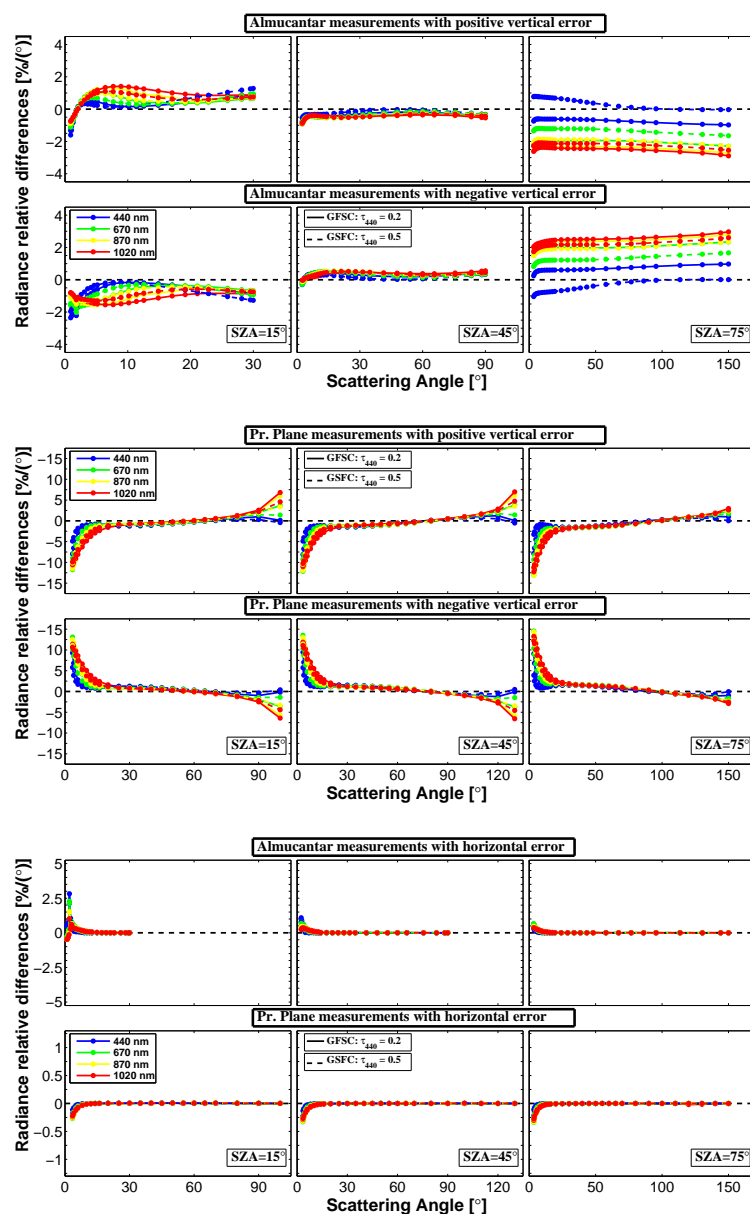


Fig. 11. Radiance relative differences obtained simulating a pointing error of 0.4° . GSFC aerosol was taken as example using two different AOD: $\tau_{440} = 0.2$ (solid line) and $\tau_{440} = 0.5$ (dashed line). Figures in the upper part correspond to vertical errors for almucantar and principal plane (four subfigures due to the plus/minus sign). On the bottom, the effects of horizontal errors are represented. From left to right, θ_s increases for the different figures.

mode of the size distribution, commented on in previous sections.

There are two ideas supporting this argument. First, the variation of the real part is minor for the 1020 nm channel, but it becomes greater as the wavelength is shortened, as short wavelengths are more affected by the fine mode particles. Needless to say, for negative errors the explanation above is valid, but changes the sign of the variations. The second proof is that the real part is more stable for the biomass burning example (more absorbing than urban), for the largest

aerosol optical depth and for the largest solar zenith angles, which were the same conditions that we found for the smallest variations in the size distributions.

If we now analyze the effect of vertical errors on almucantar measurements, we observe that the radiance relative differences (in Fig. 11), are positive for $\theta_s = 15^\circ$, negative for $\theta_s = 75^\circ$ and close to zero at $\theta_s = 45^\circ$ when the pointing error is positive. As a consequence, ω_o will increase at small scattering angles and decrease at large scattering angles. This tendency is found in the three aerosol types presented. Note

that this drift is opposite to the fictitious ω_0 cycle presented in Sect. 2.2 for almucantars.

When vertical errors are negative, there are negative differences for $\theta_s = 15^\circ$ and positive differences for $\theta_s = 75^\circ$, finding no differences again at $\theta_s = 45^\circ$. Thus, ω_0 would have the opposite behavior: reduction for small θ_s and increment for large θ_s . Therefore, negative vertical pointing errors will enlarge the fictitious daily cycle of ω_0 in almucantar retrievals. Both results are confirmed in Fig. 9.

The imaginary part of the refractive index responds in the same way as the single scattering albedo, but its variations have the opposite sign. Again, both parameters are less affected for the case of biomass burning, as its absorption is greater than in the other two cases and the aerosol load considered is larger. The real part does not suffer relevant variations at the presence of vertical error in the almucantar geometry.

Finally, we want to indicate that the optical parameters analyzed do not suffer any variations with respect to the reference cases presented in Fig. 3 for horizontal errors in both geometries.

2.6 Dependence on the finite field of view

The concept of sky radiance can be defined as the radiant flux per unit projected area and per unit solid angle coming from a specified point in the sky (McCluney, 1994). That is why, ideally, the observational solid angle should be infinitesimal. The inversion algorithms, which use radiance measurements as input, also use this approximation, considering that the instrument field of view is infinitesimal.

Nevertheless, the instruments have a finite field of view, especially in the case of the sun photometer CIMEL-318, the value of the field of view is 1.2° (Holben et al., 1998) in the actual instruments and, in old versions, 2.4° (CIMEL, personal communication, 2010).

The effect of the finite field of view on the radiance measurement in every observation point is obtained by the convolution of the viewing geometry and the angular values of the sky radiance. In Torres (2012), several tests done with the sun photometer CIMEL-318 showed that the shape of its field of view can be approximated as a cylinder. Using this result, the convolution is simplified as a surface integral of the radiance function within the field of view region. In our approach, the integral is substituted by a discrete sum considering 17 points in the field of view range around the observation point, see Fig. 12. As the areas are chosen in order to be equal, the fore-mentioned surface integral is approximated by averaging the sky radiance values obtained in the 17 selected points.

The test are done considering values of the field of view of 1.2° or 2.4° in every measurement point for the almucantar and for the principal plane geometries. As in previous analysis, the study is done using the three aerosol examples described and at five solar zenith angles (15° , 30° , 45° , 60° and 75°).

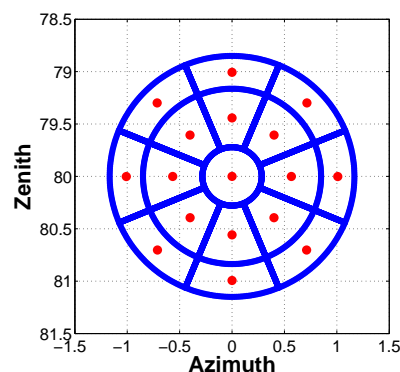


Fig. 12. Representation of the 17 point-scheme followed to simulate the effects of a finite field of view on the radiance measurements. In the example, the field of view is 2.4° and $\theta_s = 80^\circ$.

The results obtained simulating a field of view of 1.2° (non-plotted) are the same that the ones obtained in Fig. 3. It can be concluded, therefore, that the actual field of view of 1.2° does not include any variations with respect to the non-error case.

On the other hand, the results for a field of view of 2.4° indicate that the variations respect to the non-error data set are only relevant for the real part of the refractive index. Specifically, in the almucantar, the results obtained for $\theta_s = 15^\circ$ are around 3 % lower than in Fig. 3; for the rest of the solar zenith angles the differences are negligible. For the principal plane, the real part show smaller oscillations (under 3 %) but they appear for all the solar zenith angles.

3 Check of the simulations against selected stable data

In order to complete the work, we propose a parallel study with real data comparing the retrievals of principal plane and almucantar from the same three AERONET sites used during the sensitivity analysis: Mongu (Zambia, 15.25° S– 23.15° E, 1107.0 msl) is chosen for the analysis of biomass burning aerosol; GSFC (USA, 38.99° N– 76.84° W, 87.0 msl) for urban aerosol; and Solar Village (Saudi Arabia, 24.90° N– 46.40° E, 790 msl) for desert dust aerosol. We only select data that meet the next four requirements: (1) data with aerosol optical depth belonging to AERONET Level 2.0 (though we did not only use Level 2 retrievals as we are interested also in almucantar data with $\theta_s < 50^\circ$ and $\tau_a(440) < 0.4$); (2) data from those days where the ratio between the standard deviation and the average of the aerosol optical depth values is smaller than 0.1 (evaluated for the four wavelengths used by the inversion 440, 670, 870 and 1020 nm). This requirement is established in order to assure that the analysis is done for stable aerosol conditions. (3) The pairs almucantar and principal plane are selected only if both measurements took place within a maximum delay of 30 min. (4) Finally, only those days presenting at least 4

pairs matching the previous three conditions are chosen for the comparison.

Following these previous requirements, a total of 204 pairs were selected for the comparison, of which 65 pairs belong to biomass burning (top left of Table 4), 58 pairs to urban aerosol (top right in Table 4) and 81 pairs to desert dust. The latter set was divided into two subgroups as it will be commented later (Table 4 at the bottom, left and right).

The comparison for Mongu includes data from 2003 to 2009 for four different sun photometers. It is worth mentioning that we guaranteed that the data correspond to biomass burning events by the application of typical thresholds for Angstrom exponent values in biomass burning ($\alpha > 1.65$, Eck et al., 1999). As a consequence, all the days found are contained in the period from July to October. The comparison in GSFC can be seen on the top right part of Table 4. All the data selected belong to the months between June and October. As for the Mongu site, we have selected data only when $\alpha > 1.65$. The data corresponding to the comparison in Solar Village, used in order to do the analysis of desert dust aerosol, are contained at the bottom part of Table 4. The reason for splitting those data in two groups was established during the evaluation of the comparisons ALM-PPL. At this point, we observed that for some photometers (Table 4 bottom part on the left) the results presented a similar aspect to the ones obtained for the two previous aerosol types, whereas for some other photometers the comparison achieved was much worse (Table 4, bottom part on the right), especially in the size distribution (as will be shown in the next section). Nevertheless, this case presents a higher number of days with stable conditions, providing enough data to carry out the double analysis.

3.1 Size distribution

Figure 13 represents the mean and standard deviation (error bars) of the relative differences obtained for the comparison of the size distribution in the three analyzed cases: biomass burning (upper part of the figure, data from the top-left part of Table 4) urban (central part of the figure, data from the top-right part of Table 4) and desert dust (lower part of the figure, only the data from the bottom-left of Table 4).

Observing the figure, we can see how the comparisons for the three aerosol types present similar results as those obtained in the self-consistency analysis from the previous section: there is a general good agreement for radii between $0.1\ \mu\text{m}$ and $5\ \mu\text{m}$, with values of the average of the relative differences under 10 % – except for the radii around $2\ \mu\text{m}$ where the difference is a bit higher, reaching maximum values up to 20 %. Thus, these differences are a bit higher than those obtained from simulated data. At this point, the reader may remember the possibility of several error sources, such as the ones we have studied in the simulation analysis, which could provoke the increase in the discrepancy between PPL and ALM retrievals. Nevertheless, the discrepancy is still

within the interval 15–25 % which is the expected accuracy suggested by AERONET for almucantar retrievals. Finally, it should be noted that observations from all solar zenith angles have been accounted in Fig. 13; the results represent an average between retrievals with small solar zenith angles, generally with larger errors, and large solar zenith angles.

Moving to the extremes, for radii smaller than $0.1\ \mu\text{m}$ or larger than $5\ \mu\text{m}$, the comparison is much worse than in the previous analyzed region, as was expected. The relative differences are much larger, up to 60 %, but still similar to those obtained in the previous section and within the confidence interval given by AERONET for these radii (up to 100 %). The unexpected result is that these differences are positive, indicating that the values in the size distribution obtained from the almucantar are systematically lower than those obtained using the principal plane.

Among the three aerosol types, the urban aerosol shows the smallest discrepancies for fine mode; for this aerosol type, even for radii smaller than $0.1\ \mu\text{m}$ the differences are under 10 %. In the coarse mode, the smallest differences are obtained for the case of biomass burning; for this case, differences are under 22 % except for the last bin (at $15\ \mu\text{m}$) where the relative difference is 44 %. Desert dust case presents the worst-case behavior, especially in the coarse mode, where for several bins the relative differences exceed 40 %, reaching the maximum of 60 % at $11.4\ \mu\text{m}$.

3.2 Optical parameters

Table 5 contains the mean values and the standard deviations obtained for the single scattering albedo and the refractive index in the analyzed days using only almucantar geometry. The values obtained for the three aerosol cases are similar to those presented in Table 1 (Table 1 in Dubovik et al., 2002). For instance, $\omega(440) = 0.85$, corresponding to the analysis of the biomass burning, is comparable to the one used in the simulation analysis, $\omega(440) = 0.88$ (Table 1).

Returning to the comparison between the principal plane and almucantar retrievals, the results for the single scattering albedo are shown in Fig. 14. The mean of the differences between both inversions are plotted against the wavelength for the three aerosol cases analyzed: biomass burning (gray), urban (blue) and desert dust (orange). The standard deviation of the differences is represented using the error bar. As it can be seen in the plot, the average of the differences is under 0.01 for the three analyzed cases and for the four wavelengths, reaching the highest value (0.007) at 440 nm for the desert dust. On the other hand, the standard deviation is under 0.01 for all the wavelengths in the biomass burning, between 0.01–0.015 for urban aerosol, and slightly higher for the desert dust aerosol (where values around 0.02 are obtained). Nevertheless, this result is due to the effect of the problem regarding the almucantar angle coverage: if we reduce the analyses to those cases in which $\theta_s > 50^\circ$, the standard deviation reduces its values considerably, especially for the desert

Table 4. Description of the data used for the comparison between almucantar and principal plane retrievals for the different sites.

Biomass burning (Mongu)					Urban (GSFC)				
Photo.	Date	No. pairs	$\langle \tau_a(440) \rangle$	$\langle \alpha \rangle$	Photo.	Date	No. pairs	$\langle \tau_a(440) \rangle$	$\langle \alpha \rangle$
#36	09-08-2009	4	0.34	2.00	#101(1)	21-10-2001	6	0.14	1.76
	12-08-2009	7	0.63	1.89		24-10-2001	5	0.24	1.90
	16-07-2009	5	0.71	1.85	#101(2)	17-07-2002	6	0.44	1.88
#65	01-10-2004	4	0.37	1.72		13-08-2002	4	1.15	1.80
	25-07-2004	6	0.61	1.75	#89(1)	23-06-2003	4	0.33	1.75
	17-09-2004	6	0.78	1.83		29-06-2003	4	0.71	1.65
#11	30-07-2003	5	0.45	1.92	#94(1)	24-06-2005	6	0.48	1.66
	18-08-2003	6	0.68	1.79		02-08-2005	4	0.38	1.89
	14-08-2003	6	0.72	1.66	#89(2)	08-09-2007	5	0.49	1.83
#152	02-08-2006	6	0.42	1.71		26-09-2007	4	0.59	1.89
	25-07-2006	4	0.53	1.79	#94(2)	13-10-2007	5	0.14	1.67
	18-08-2006	6	0.73	1.80		17-10-2007	5	0.40	1.88
Desert dust 1 (Solar Village)					Desert dust 2 (Solar Village)				
Photo.	Date	No. pairs	$\langle \tau_a(440) \rangle$	$\langle \alpha \rangle$	Photo.	Date	No. pairs	$\langle \tau_a(440) \rangle$	$\langle \alpha \rangle$
#65	05-03-2003	7	0.33	0.25	#233	25-04-2008	7	0.36	0.25
	02-04-2003	5	0.48	0.20		26-04-2008	4	0.43	0.28
	11-09-2002	5	0.64	0.55		28-05-2008	6	0.51	0.25
#185	20-10-2005	5	0.32	0.49	#33	04-06-2004	7	0.33	0.55
	19-10-2005	6	0.41	0.46		22-05-2004	4	0.46	0.16
	19-06-2006	4	0.54	0.44		18-05-2004	5	0.71	0.11
#95	07-03-2011	5	0.38	0.30					
	09-10-2010	5	0.48	0.59					
	26-08-2010	6	0.73	0.73					

Table 5. Mean values and standard deviations obtained for the single scattering albedo and the refractive index in the analyzed days using only almucantar geometry.

$\omega(\lambda)$						$n(\lambda)$				$k(\lambda)$			
Wavelength [nm]		440	670	870	1020	440	670	870	1020	440	670	870	1020
Bio. burn. (Mongu)	mean	0.85	0.81	0.78	0.76	1.53	1.53	1.54	1.54	0.032	0.032	0.030	0.027
	std	0.03	0.05	0.05	0.05	0.04	0.03	0.03	0.03	0.012	0.013	0.012	0.011
Urban (GSFC)	mean	0.96	0.94	0.93	0.93	1.40	1.41	1.41	1.42	0.005	0.005	0.005	0.005
	std	0.02	0.03	0.04	0.04	0.05	0.05	0.05	0.05	0.003	0.003	0.003	0.003
Desert dust (Solar Vil.)	mean	0.90	0.92	0.94	0.94	1.51	1.54	1.54	1.54	0.006	0.004	0.004	0.004
	std	0.02	0.03	0.03	0.03	0.05	0.03	0.03	0.03	0.003	0.003	0.002	0.002

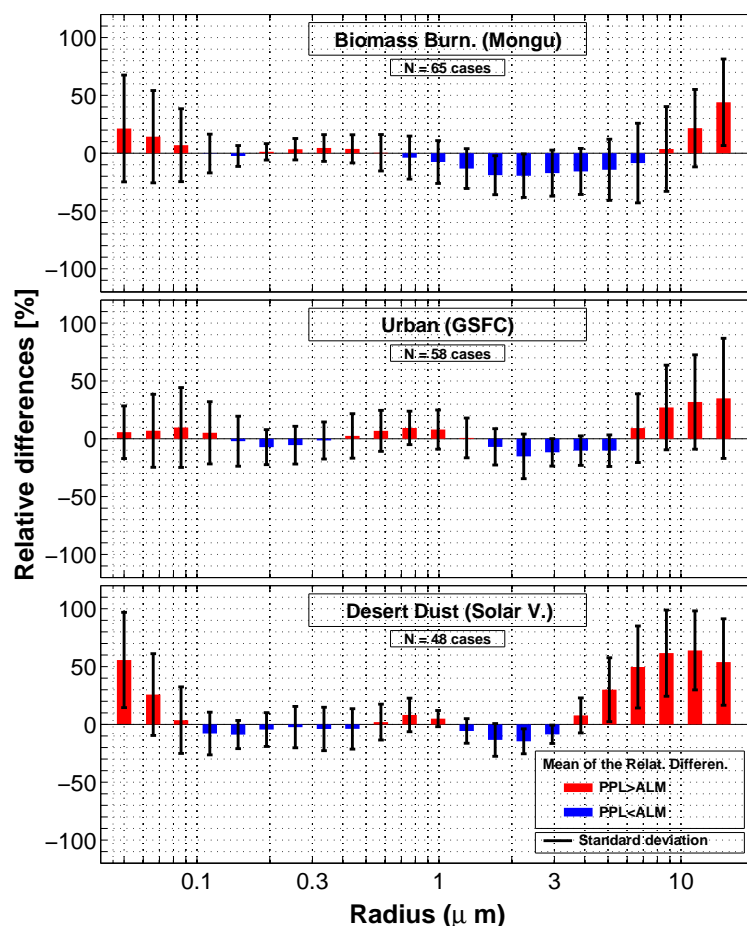


Fig. 13. Relative differences found in the size distribution between the inversion obtained by almucantar and principal planes for the three analyzed cases (data description in Table 4): biomass burning (upper part of the figure), urban (central part of the figure), and desert dust (lower part of the figure, only data from the first set (called desert dust 1)).

dust where $\sigma = 0.01$. It should be mentioned that the uncertainty given by AERONET for ω_0 is 0.03 (http://aeronet.gsfc.nasa.gov/new_web/Documents/inversions.pdf), which highlights the extraordinary agreement obtained here when the atmosphere is stable and homogeneous.

Figure 15 shows the results for the real part of the refractive index. The averaged values of the difference for biomass burning and urban aerosol are lower than 0.01, indicating that there is no shared tendency for principal plane and almucantar differences; on the contrary, the difference for the desert dust is about 0.03, or in other words, the values of the real part of the refractive index retrieved using principal plane are, on average, significantly higher than those obtained using almucantar for the desert dust. The standard deviation, with a value about 0.03 for the three cases, does not depend on the aerosol type. These results are not improved when the study is limited to $\theta_s > 50^\circ$. Nonetheless, the accuracy given for this parameter is 0.03 for biomass burning and urban and slightly higher, 0.05, for desert dust; therefore, the results are within this interval.

Figure 16 depicts the averages and the standard deviations of the absolute differences for the imaginary part of the refractive index. Contrary to the previous cases, the highest standard deviations of the absolute differences are reached for the biomass burning aerosol presenting values around 0.003. On the other hand, the values for desert dust and urban aerosol are enclosed between 0.0015 and 0.0023. It should be remembered (Table 5), that the absolute values of the imaginary part of the refractive index for the biomass burning are one order of magnitude higher than those for the desert dust and urban aerosol. Therefore, in relative terms, the best comparison is again obtained for biomass burning case. It can be noted the opposite sign for the differences of imaginary part of the refractive index and the single scattering albedo. This fact is justified by the strong anticorrelation between both magnitudes. Using Table 5, we observe that the average of the differences (principal plane vs. almucantar) of the imaginary part of the refractive index have a maximum of 13 % for the urban aerosol, 9 % for the desert dust aerosol, and 4 % for biomass burning.

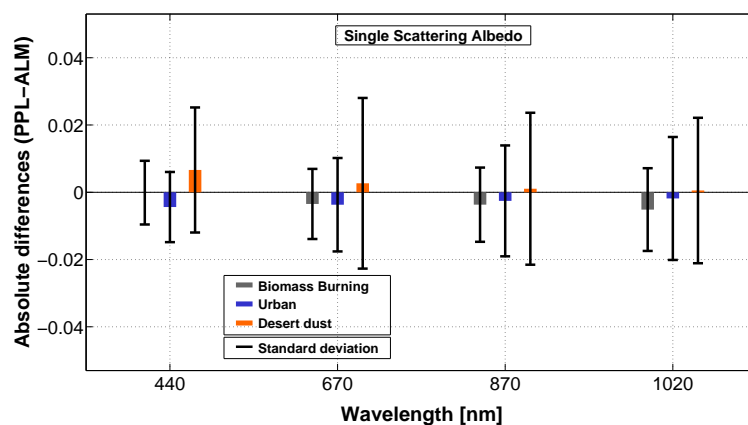


Fig. 14. Absolute differences (with sign) found in the single scattering albedo between the inversion obtained by almucantar and principal planes for the three analyzed cases (Table 4): biomass burning (gray), urban (blue) and desert dust (orange, only data from the first set (called desert dust 1)). Bars indicate the standard deviation of the differences.

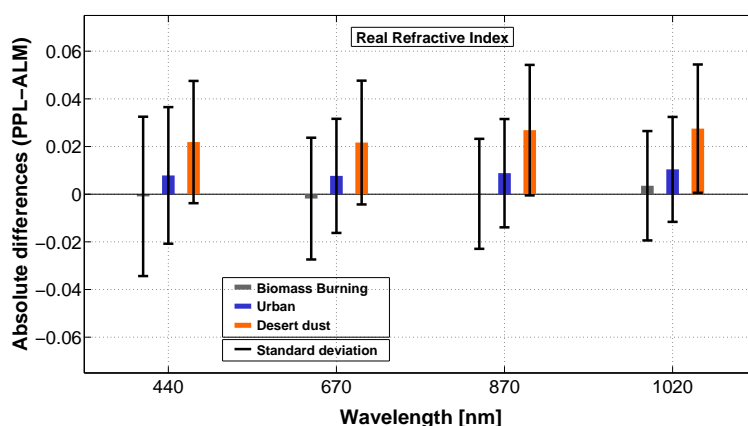


Fig. 15. Absolute differences (with sign) found in the real part of the refractive index between the inversion obtained by almucantar and that obtained by principal planes for the three analyzed cases (Table 4): biomass burning (gray), urban (blue) and desert dust (orange, only data from the first set (called desert dust 1)). Bars indicate the standard deviation of the differences.

3.3 Desert dust 2: data subset with larger discrepancies

As was just shown, the comparisons obtained from desert dust aerosol have a larger error than the error comparisons obtained from the other aerosol types. Moreover, for some photometers these differences were substantially larger. This was the case for photometers #233 and #33 (called desert dust 2 subset); the results obtained for these photometers were systematically worse for every single pair of data compared.

Looking at Table 4, it can be seen that the mean Angstrom exponent of desert dust 1 spans from 0.20 to 0.73, while for desert dust 2 it ranges from 0.11 to 0.55. On the other hand, in Table 6, for each mode of the volume particle size distribution $[dV(r)/d\ln r]$, mean values of the particle volume concentration, the median radius, and the standard deviation (obtained only using almucantar inversions) are represented

for both desert dust sets. The values observed are very similar for both groups, showing that, apparently, the higher alpha values observed in desert dust 1 does not seem to have any consequences in the retrieved aerosol size distribution. Note here as well, that the values of the median radius and the standard deviation for the coarse mode (r_{vc} and σ_{vc}) shown in Table 1 were 2.32 and 0.6, which are in a perfect agreement with the ones obtained in the two subgroups here.

The upper chart in Fig. 17 contains the average of the relative differences and the standard deviation obtained from the comparison between the retrievals using principal plane and almucantar in the subset desert dust 2. The most outstanding result is the strong increase of the values in the extremes ($r < 0.1 \mu\text{m}$ and $r > 5 \mu\text{m}$) compared to the previously analyzed cases. For the coarse mode, the average differences exceed 100 %. However, the averaged values for the mid-range are similar to the previous cases, being under 20 %. We find

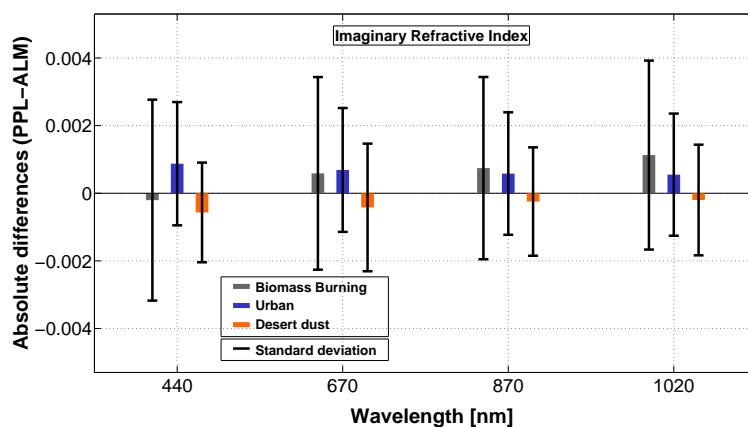


Fig. 16. Absolute differences (with sign) found in the imaginary part of the refractive index between the inversion obtained by almucantar and principal planes for the three analyzed cases (Table 4): biomass burning (gray bar) urban (blue bar) and desert dust (orange bar, only data from the first set (called desert dust 1)).

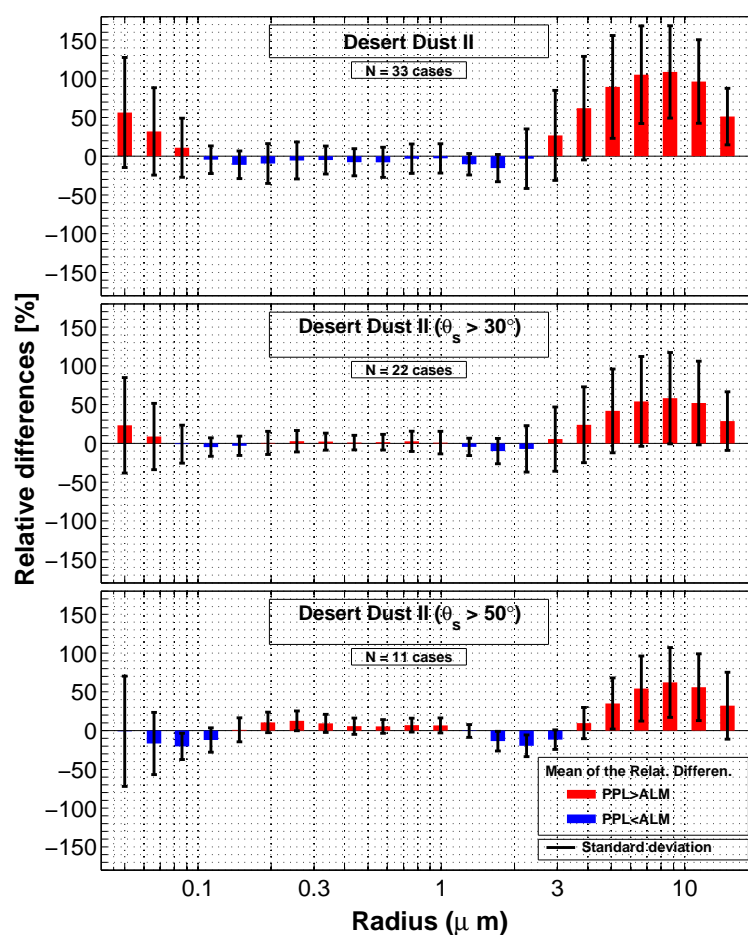


Fig. 17. Relative differences found in the size distribution between the inversion obtained by almucantar and principal planes for the photometers #233 and #33 in Solar Village site (data description in Table 4 case desert dust 2). The upper chart contains a comparison for the whole data set, while the central and the bottom chart contain comparisons only for those data with the solar zenith angle larger than 30° and 50° , respectively.

Table 6. Mean values of the particle volume concentration C_{Vi} , the median radius r_{Vi} , and the standard deviation σ_{Vi} for each mode of the volume particle size distribution for the defined groups desert dust 1 and desert dust 2.

	C_{Vf}	r_{Vf}	σ_{Vf}	C_{Vc}	r_{Vc}	σ_{Vc}
Desert dust 1	0.03 ± 0.02	0.14 ± 0.02	0.51 ± 0.07	0.25 ± 0.07	2.33 ± 0.24	0.62 ± 0.03
Desert dust 2	0.03 ± 0.01	0.17 ± 0.04	0.61 ± 0.07	0.23 ± 0.09	1.95 ± 0.33	0.57 ± 0.06

Table 7. Mean values and the standard deviations of the absolute differences (with sign principal plane minus almucantar) for the optical parameters found for the data set desert dust 2.

		Total differences											
		$\omega(\lambda)$				$n(\lambda)$				$k(\lambda)$			
Wavelength [nm]		440	670	870	1020	440	670	870	1020	440	670	870	1020
All data	mean	0.03	0.03	0.03	0.02	0.03	0.03	0.03	0.03	−0.004	−0.003	−0.003	−0.002
	std	0.05	0.05	0.04	0.03	0.06	0.05	0.05	0.06	0.006	0.005	0.004	0.004
$\theta_s > 30^\circ$	mean	0.01	0.00	0.00	0.00	0.01	0.01	0.01	0.01	−0.001	−0.000	−0.000	−0.000
	std	0.02	0.02	0.02	0.01	0.02	0.02	0.02	0.02	0.003	0.002	0.002	0.002
$\theta_s > 50^\circ$	mean	−0.00	−0.01	−0.00	−0.00	0.01	0.01	0.01	0.01	0.001	0.000	0.000	0.000
	std	0.01	0.01	0.01	0.01	0.02	0.02	0.02	0.02	0.001	0.001	0.001	0.001

an exception for the radii between 3 μm and 5 μm , where the differences, affected by the strong increase in the extremes, present values up to 60 %. In the same way, the standard deviation shows a similar behavior, doubling its value in the extremes (from 30–40 % it increases to 60 %) but keeping around 20 % in the central part.

The central and the bottom chart of Fig. 17 correspond to the same analysis (photometers #233 and #33) but are limited to those cases where the solar zenith angle is larger than 30° and 50° , respectively. As can be seen, both limitations improve the comparison considerably. The comparison for solar zenith angles larger than 30° eliminates 11 pairs of data (from 33 to 22) and the results, especially the average value of the relative differences, are diminished, reaching similar values to the ones obtained for the photometers classed in the subset Desert Dust I. Again, another 11 pairs of data disappear when the limitation is extended to $\theta_s > 50^\circ$; under this criterion, the average values do not suffer any improvements, but the standard deviations are appreciably lower, especially for $r > 3 \mu\text{m}$.

Continuing with the analysis of the data set desert dust 2, the results for the optical parameters are shown in Table 7. Averaged values and the standard deviations of the differences between the retrievals of principal plane and almucantar are presented for all data (upper part of the Table 7), those data with $\theta_s > 30^\circ$ (central part of the Table 7) and only for those cases where $\theta_s > 50^\circ$ (bottom part of the Table 7).

The means of the differences observed for the whole data set are, in general, considerably larger than the values observed in the data set desert dust 1 (Figs. 14–16). Thus, averaged differences are about three times larger for the single

scattering albedo and for the imaginary part of the refractive index in this data set than those obtained for the desert dust 1. In the same manner, the values of the standard deviation are typically twice as large.

On the other hand, the real part of the refractive index presents similar means of the differences as those obtained for the data set desert dust 1. Nevertheless, the values of the standard deviation for this parameter are again twice as large as the ones shown in Fig. 15.

Once we limit the study to those data with $\theta_s > 30^\circ$ and $\theta_s > 50^\circ$, the differences descend for the three parameters analyzed. The values of the differences for both restricted data sets (presented in the central and bottom part of Table 7) are similar to the ones obtained in the study for desert dust 1.

It should be noted here that, apart from the error sources considered throughout the study, the AOD errors are of importance in the retrieving process (Dubovik et al., 2000). We have not focused on them in the present study, since in principle the AOD measurements are equivalent to the PPL or ALM geometries. However, if AOD errors are significant, they may have different effects on aerosol retrievals using PPL and ALM observations, especially in those cases with larger differences in the information content, i.e., for small solar zenith angles where the scattering angle coverage in the almucantar is significantly smaller. Furthermore, the error in AOD due to calibration is proportional to $1/m$ (m = optical air mass; $m \sim 1/\cos(\text{SZA})$; see Hamonou et al., 1999) which particularly enlarges the AOD errors for short solar zenith angles. The combination of both factors can explain the better agreement between the two geometries at larger SZA, where the AOD is more accurate. In fact, some uncertainties in the

AOD calibration have been found in the set desert dust 2 data (e.g., spectral crossovers of 440 and 500 nm).

4 Discussion

PPL retrievals are not available for the use of the wider scientific community and most of the studies presented in the literature where aerosol microphysical properties are retrieved using Sun and sky radiance measurements have been done exclusively using almucantar measurements (Holben et al., 2001; Smirnov et al., 2002; Dubovik et al., 2002; Eck et al., 2010; Giles et al., 2012, to cite some). One of the reasons for such situation is that aerosol community generally has higher confidence in the almucantar retrievals. Significant efforts have been undertaken in order to understand the potential of PPL retrievals and compare them with ALM data – for instance, in the AERONET project, internal research activities have been developed (Alexander Sinyuk and Brent Holben, personal communication). However, no comprehensive analysis of the expected differences of almucantar retrievals with respect to principal planes is available in open-access literature. As a result, for the wider scientific community, the positive potential and shortcomings of using PPL aerosol remains unclear, in particular since the inversion strategy does not reveal any clear preference in the geometry of the radiance measurement. Therefore, the purpose of this study is to summarize and document the sensitivity of aerosol retrievals to geometrical configurations of observations with a focus on detailed comparative analysis of PPL and ALM retrievals.

One of the main practical reasons for preferring the aerosol retrieval from almucantar observations is the great advantage provided by the symmetry existing in the almucantar measurements. First, taking the average of left and right branches results in more stable measurements and helps to reduce the error effects. In addition, the averaging process also provides a more representative spatial (angular) distribution of sky radiances, diminishing the effect of the aerosol inhomogeneity. Moreover, the symmetry allows one to perform a cloud screening that can not be automatically assessed from principal plane data. These facts and others potentially compromise the accuracy of PPL retrievals (Holben et al., 1998, 2006; Dubovik et al., 2000), and consequentially prevented the AERONET project from releasing PPL retrieval for public use since the reliability of the data is one of the primary objectives of the AERONET network.

Indeed, during the present analysis, both the sensitivity tests with the introduced modeled errors and the analysis of data acquired under stable conditions confirmed the greater reliability that is generally assumed regarding almucantar retrievals. It has been shown that the average between the left and right branches in the almucantar largely diminishes the consequences of possible pointing offsets in the instruments, while for the principal plane the consequences of such errors are more significant. Furthermore, almucantar retrievals have

shown less dependency on the aerosol vertical distribution, as generally expected from theoretical considerations.

On the other hand, the retrievals from almucantars taken at high solar elevation show significant decreases in accuracy for most of the retrieved aerosol parameters (Fig. 3). This result was already well discussed in Dubovik et al. (2000) and is accounted for in the quality selection criteria (summarized in Dubovik et al., 2002) and adapted for Level 2 retrieval in AERONET version 2, where only retrievals with $\theta_s > 50^\circ$ are accepted. Therefore, one of the immediate consequences of using exclusively almucantar geometry is the lack of high accuracy aerosol retrievals during the middle of the day (except at high latitudes and in wintertime at subtropical to mid-latitudes), which are highly desirable for the various aerosol studies. However, in the same simulation analysis (Fig. 3) the principal plane retrievals remain stable over the course of the day due to their larger angular scattering coverage.

The sensitivity tests and the real data analysis conducted in this study show sufficiently high consistency between principal plane and almucantar retrievals, and this fact supports the idea of using principal plane inversions to complement almucantar retrievals in some specific cases, such as ground-based campaigns or the study of aerosol events. Nevertheless, we should note that in both tests we have used quite selective data: in the first analysis, the data have been synthetically generated and in the real data analysis we have manually inspected the radiance data and maintained quite restrictive conditions low AOD daily variation, etc.; see Sect. 3). Therefore, the use of principal plane data can only be recommended if a reliable cloud-screening procedure is developed for PPL observations or for those cases when the manual inspection of the data is possible.

5 Conclusions

The simulated studies carried out using synthetic data from a climatology analyses of the sites Solar Village, GSFC, and Mongu have confirmed that the symmetry existing for the almucantar geometry confers a greater robustness of the aerosol retrievals in presence of various systematic uncertainties. In fact, the straightforward symmetry check used in aerosol quality screening seemed to be a very efficient and practical procedure to eliminate sky inhomogeneities and reduce some of possible instrumental biases. For example, the present study has showed that if pointing errors are present, the consequences for principal plane retrievals are much larger than for almucantar retrievals. Only in an ideal situation of homogeneous atmosphere when no extra errors were introduced, would data from the principal plane geometry provide more reliable results than those from almucantar for high Sun observation due to lower information content in the almucantar radiances, where the range of observed scattering angles is substantially reduced.

An analysis of data during stable atmospheric conditions has been developed for the same three sites using a set of selection criteria (see Sect. 3). The comparison between principal plane and almucantar retrievals obtained in this analysis has shown that the differences in the products are, in general, within AERONET-estimated uncertainties for almucantar retrievals. The differences between the retrievals of the size distribution are generally under 10 % for radii between 0.1 μm and 5 μm . Outside this size range, the differences can be as large as 50 % and mostly positive (i.e., principal plane inversion results in larger volume concentrations than the almucantar). This result was expected due to the loss of sensitivity of the retrievals to particles of those sizes for the wavelengths used in AERONET and it was previously obtained with simulated data (similar result also in Dubovik et al., 2000).

These high differences in the extremes have almost no impact on other aerosol properties retrieved, such as the aerosol optical depth or the optical parameters. Indeed, even though there are differences over 50 % in the edge bins of the size distribution, the subsequent differences in the optical parameters are almost negligible (e.g., absolute differences in the single scattering albedo under 0.01 for all cases).

On the other hand, the comparison between the almucantar and principal plane retrievals in the subset desert dust 2 are systematically worse than those obtained in the other analyzed cases, in particular the subset desert dust 1. The cause of these higher discrepancies has not been fully identified, however, it is reasonable to expect different tendencies in the results of PPL-ALM retrieval comparisons in the two subsets desert dust 1 and 2 because of the different instrument performance (in this case photometers #233 and #33). Indeed, instrumental issues related to AOD accuracy may cause discrepancies at low solar zenith angles. Another possible explanation is the different aerosol average conditions. In particular, the mean Angstrom exponent in subset desert dust 1 (about 0.6) is higher than for pure desert dust and indicates the presence of a significant fine mode fraction. Alternatively, the subset desert dust 2 (with mean Angstrom exponent of 0.3) is representative of nearly pure dust.

Finally, this last group has been reanalyzed, limiting the data set to large $\theta_s > 50^\circ$, which is in agreement with the well-known AERONET level 2.0 criterion about SZA. This threshold significantly reduces the AOD uncertainty related to calibration (e.g., due to filter degradation) and therefore improves the retrieval accuracy. In addition, the analysis for different errors in Sect. 2 also indicates that the differences between almucantar and principal plane are smaller for larger θ_s . Thus, the differences in the scattering angle range in the two geometries could amplify the discrepancies obtained between the retrievals if they are associated with instrumental problems. As a result, significant improvements have been observed in the retrieval comparison of PPL vs. ALM when limiting the data set to large $\theta_s (> 50^\circ)$; one observes the same typical differences as in the other data subset, desert dust 1.

Acknowledgements. We thank the AERONET principal investigators and site managers at sites Solar Village (Naif Al-Abbadi, Steve Wilcox), GSFC (Mikhail Sorokin, Brent Holben) and Mongu (Mukufute Mukulabai, Brent Holben). We thank the AERONET, PHOTONS, RIMA and WRC staff for their scientific and technical support. We acknowledge AERONET team members for calibrating and maintaining instrumentation and processing data. We especially thank I. Slutsker for providing us with useful tools for data treatment and Brent Holben for his scientific support. The authors also thank T. Eck and the anonymous reviewer for comments that led to a significant improvement to the paper. Financial support was provided by the Spanish CICYT (CGL2009-09740 and CGL2011-23413, CGL2011-13085-E). The research leading to these results was supported by funding from the European Union Seventh Framework Programme (FP7/2007-2013) under grant agreement no. 262254 [ACTRIS]. We also thank the Environmental Council of the CyL Regional Government (Consejería de Medio Ambiente, Junta de Castilla y León) for supporting this research. The publication of this article is financed by CNRS-INSU.

Edited by: D. Tanre



The publication of this article is financed by CNRS-INSU.

References

- Bohren, C. and Huffman, D.: Absorption and Scattering of Light by Small Particles, John Wiley & Sons Inc, doi:10.1002/9783527618156, 1983.
- Cox, C. and Munk, W.: Measurement of the roughness of the sea surface from photographs of the suns glitter, *J. Opt. Soc. Am.*, 44, 838–850, doi:10.1364/JOSA.44.000838, 1954.
- D'Almeida, G., Koepke, P., and Shettle, E.: Atmospheric Aerosols: Global Climatology and Radiative Characteristics, A. Deepak Publishing, 1991.
- Dubovik, O. and King, M.: A flexible inversion algorithm for retrieval of aerosol optical properties from Sun and sky radiance measurements, *J. Geophys. Res.-Atmos.*, 105, 20673–20696, doi:10.1029/2000JD900282, 2000.
- Dubovik, O., Smirnov, A., Holben, B., King, M., Kaufman, Y., Eck, T., and Slutsker, I.: Accuracy assessments of aerosol optical properties retrieved from Aerosol Robotic Network (AERONET) Sun and sky radiance measurements, *J. Geophys. Res.-Atmos.*, 105, 9791–9806, doi:10.1029/2000JD900040, 2000.
- Dubovik, O., Holben, B., Eck, T., Smirnov, A., Kaufman, Y., King, M., Tanre, D., and Slutsker, I.: Variability of absorption and optical properties of key aerosol types observed in worldwide locations, *J. Atmos. Sci.*, 59, 590–608, doi:10.1175/1520-0469(2002)059<0590:VOAOP>2.0.CO;2, 2002.
- Dubovik, O., Sinyuk, A., Lapyonok, T., Holben, B. N., Mishchenko, M., Yang, P., Eck, T., Volten, H., Munoz, O., Veihelmann, B., Van Der Zande, W. J., Leon, J., Sorokin, M., and Slutsker, I.: Application of spheroid models to account for aerosol particle

- nonsphericity in remote sensing of desert dust, *J. Geophys. Res.-Atmos.*, 111, D11208, doi:10.1029/2005JD006619, 2006.
- Eck, T., Holben, B., Reid, J., Dubovik, O., Smirnov, A., O'Neill, N., Slutsker, I., and Kinne, S.: Wavelength dependence of the optical depth of biomass burning, urban, and desert dust aerosols, *J. Geophys. Res.-Atmos.*, 104, 31 333–31 349, doi:10.1029/1999JD900923, 1999.
- Eck, T. F., Holben, B. N., Reid, J. S., Sinyuk, A., Dubovik, O., Smirnov, A., Giles, D., O'Neill, N. T., Tsay, S.-C., Ji, Q., Al Mandous, A., Ramzan Khan, M., Reid, E. A., Schafer, J. S., Sorokine, M., Newcomb, W., and Slutsker, I.: Spatial and temporal variability of column-integrated aerosol optical properties in the southern Arabian Gulf and United Arab Emirates in summer, *J. Geophys. Res.-Atmos.*, 113, D01204, doi:10.1029/2007JD008944, 2008.
- Eck, T. F., Holben, B. N., Sinyuk, A., Pinker, R. T., Goloub, P., Chen, H., Chatenet, B., Li, Z., Singh, R. P., Tripathi, S. N., Reid, J. S., Giles, D. M., Dubovik, O., O'Neill, N. T., Smirnov, A., Wang, P., and Xia, X.: Climatological aspects of the optical properties of fine/coarse mode aerosol mixtures, *J. Geophys. Res. Atmos.*, 115, D19205, doi:10.1029/2010JD014002, 2010.
- Elterman, L.: Aerosol Measurements in the Troposphere and Stratosphere, *Appl. Optics*, 5, 1769–1775, doi:10.1364/AO.5.001769, 1966.
- Giles, D. M., Holben, B. N., Eck, T. F., Sinyuk, A., Smirnov, A., Slutsker, I., Dickerson, R. R., Thompson, A. M., and Schafer, J. S.: An analysis of AERONET aerosol absorption properties and classifications representative of aerosol source regions, *J. Geophys. Res.-Atmos.*, 117, D17203, doi:10.1029/2012JD018127, 2012.
- Hamonou, E., Chazette, P., Balis, D., Dulac, F., Schneider, X., Galani, E., Ancellet, G., and Papayannis, A.: Characterization of the vertical structure of Saharan dust export to the Mediterranean basin, *J. Geophys. Res.-Atmos.*, 104, 22257–22270, doi:10.1029/1999JD900257, 1999.
- Holben, B., Eck, T., Slutsker, I., Tanre, D., Buis, J., Setzer, A., Vermote, E., Reagan, J., Kaufman, Y., Nakajima, T., Lavenue, F., Jankowiak, I., and Smirnov, A.: AERONET – A federated instrument network and data archive for aerosol characterization, *Remote Sens. Environ.*, 66, 1–16, doi:10.1016/S0034-4257(98)00031-5, 1998.
- Holben, B., Tanre, D., Smirnov, A., Eck, T., Slutsker, I., Abuhassan, N., Newcomb, W., Schafer, J., Chatenet, B., Lavenue, F., Kaufman, Y., Castle, J., Setzer, A., Markham, B., Clark, D., Frouin, R., Halthore, R., Karneli, A., O'Neill, N., Pietras, C., Pinker, R., Voss, K., and Zibordi, G.: An emerging ground-based aerosol climatology: Aerosol optical depth from AERONET, *J. Geophys. Res.-Atmos.*, 106, 12067–12097, doi:10.1029/2001JD900014, 2001.
- Holben, B. N., Eck, T. F., Slutsker, I., Smirnov, A., Sinyuk, A., Schafer, J., Giles, D., and Dubovik, O.: AERONET's Version 2.0 quality assurance criteria, in: *Remote Sensing of the Atmosphere and Clouds*, edited by: Tsay, S., Nakajima, T., Singh, R., and Sridharan, R., Vol. 6408 of *Proc. SPIE*, p. Q4080, Conference on Remote Sensing of the Atmosphere and Clouds, Goa, India, 13–16 November, doi:10.1117/12.706524, 2006.
- Kaufman, Y., Tanre, D., Holben, B., Mattoo, S., Remer, L., Eck, T., Vaughan, J., and Chatenet, B.: Aerosol radiative impact on spectral solar flux at the surface, derived from principal-plane sky measurements, *J. Atmos. Sci.*, 59, 635–646, doi:10.1175/1520-0469(2002)059<0635:AROSS>2.0.CO;2, 2002.
- Li, Z., Goloub, P., Dubovik, O., Blarel, L., Zhang, W., Podvin, T., Sinyuk, A., Sorokin, M., Chen, H., Holben, B., Tanr, D., Canini, M., and Buis, J.-P.: Improvements for ground-based remote sensing of atmospheric aerosol properties by additional polarimetric measurements, *J. Quant. Spectrosc. Ra.*, 110, 1954–1961, doi:10.1016/j.jqsrt.2009.04.009, 2009.
- Litvinov, P., Hasekamp, O., and Cairns, B.: Models for surface reflection of radiance and polarized radiance: Comparison with airborne multi-angle photopolarimetric measurements and implications for modeling top-of-atmosphere measurements, *Remote Sens. Environ.*, 115, 781–792, doi:10.1016/j.rse.2010.11.005, 2011.
- Lopatin, A., Dubovik, O., Chaikovsky, A., Goloub, P., Lapyonok, T., Tanré, D., and Litvinov, P.: Enhancement of aerosol characterization using synergy of lidar and sun-photometer coincident observations: the GARRLiC algorithm, *Atmos. Meas. Tech.*, 6, 2065–2088, doi:10.5194/amt-6-2065-2013, 2013.
- Lucht, W. and Roujean, J.: Considerations in the parametric modeling of BRDF and albedo from multiangular satellite sensor observations, *Remote Sens. Rev.*, 18, 343–379, doi:10.1080/02757250009532395, 2000.
- McCluney, R.: *Introduction to Radiometry and Photometry*, Artech Houses Inc., Optoelectronics Library, 424 pp., 1994.
- Moody, E. G., King, M. D., Platnick, S., Schaaf, C. B., and Gao, F.: Spatially complete global spectral surface albedos: Value-added datasets derived from Terra MODIS land products, *IEEE T. Geosci. Remote*, 43, 144–158, 2005.
- Nakajima, T., Tanaka, M., and Yamauchi, T.: Retrieval of the optical-properties of aerosols from aureola and extinction data, *Appl. Optics*, 22, 2951–2959, 1983.
- Nakajima, T., Tonna, G., Rao, R., Boi, P., Kaufman, Y., and Holben, B.: Use of sky brightness measurements from ground for remote sensing of particulate polydispersions, *Appl. Optics*, 35, 2672–2686, doi:10.1364/AO.35.002672, 1996.
- Olmo, F., Quirantes, A., Lara, V., Lyamani, H., and Alados-Arboledas, L.: Aerosol optical properties assessed by an inversion method using the solar principal plane for non-spherical particles, *J. Quant. Spectrosc. Ra.*, 109, 1504–1516, 2008.
- Roujean, J.-L., Leroy, M., and Deschamps, P.-Y.: A bidirectional reflectance model of the Earth's surface for the correction of remote sensing data, *J. Geophys. Res.-Atmos.*, 97, 20455–20468, doi:10.1029/92JD01411, 1992.
- Sinyuk, A., Dubovik, O., Holben, B., Eck, T. F., Breon, F.-M., Martonchik, J., Kahn, R., Diner, D. J., Vermote, E. F., Roger, J.-C., Lapyonok, T., and Slutsker, I.: Simultaneous retrieval of aerosol and surface properties from a combination of AERONET and satellite data, *Remote Sens. Environ.*, 107, 90–108, doi:10.1016/j.rse.2006.07.022, 2007.
- Smirnov, A., Holben, B., Eck, T., Slutsker, I., Chatenet, B., and Pinker, R.: Diurnal variability of aerosol optical depth observed at AERONET (Aerosol Robotic Network) sites, *Geophys. Res. Lett.*, 29, 2115, doi:10.1029/2002GL016305, 2002.
- Solomon, S., Qin, D., Manning, M., Chen, Z., Marquis, M., Averyt, K., Tignor, M., and Miller, H. L.: Technical Summary, in: *Climate Change 2007: The Physical Science Basis Contribution of Working Group I to the Fourth Assessment Report of the*

- Intergovernmental Panel on Climate Change, Cambridge University Press, 2007.
- Takamura, T. and Nakajima, T.: Overview of SKYNET and its activities, *Opt. Pura Apl.*, 37, 3303–3308, 2004.
- Torres, B.: Study on the influence of different error sources on sky radiance measurements and inversion-derived aerosol products in the frame of AERONET, Ph.D. thesis, Universidad de Valladolid, 2012.
- Torres, B., Toledano, C., Berjón, A., Fuertes, D., Molina, V., Gonzalez, R., Canini, M., Cachorro, V. E., Goloub, P., Podvin, T., Blarel, L., Dubovik, O., Bennouna, Y., and de Frutos, A. M.: Measurements on pointing error and field of view of Cimel-318 Sun photometers in the scope of AERONET, *Atmos. Meas. Tech.*, 6, 2207–2220, doi:10.5194/amt-6-2207-2013, 2013.
- Wanner, W., Li, X., and Strahler, A. H.: On the derivation of kernels for kernel-driven models of bidirectional reflectance, *J. Geophys. Res.-Atmos.*, 100, 21077–21089, doi:10.1029/95JD02371, 1995.
- Wehrli, C.: GAW-PFR: A network of Aerosol Optical Depth observations with Precision Filter Radiometers. In: WMO/GAW Experts workshop on a global surface based network for long term observations of column aerosol optical properties, Tech. rep., GAW Report No. 162, WMO TD No. 1287, <ftp://ftp.wmo.int/Documents/PublicWeb/arep/gaw/gaw162.pdf>, 2005.
- Willeke, K. and Baron, P.: Aerosol measurement: principles, techniques, and applications, New York: Van Nostrand Reinhold, 1993.